Modern Scattering-Type Scanning Near-field Optical Microscope

Xinzhong Chen[1], Ryan Mescall[1], Debo Hu[2], Qing Dai[2*], D. N. Basov[3*], Mengkun Liu[1*]

1. Department of Physics, Stony Brook University, Stony Brook, New York 11794, USA
2. Division of Nanophotonics, CAS Center for Excellence in Nanoscience, National Center for Nanoscience and Technology, Beijing, P.R. China, 100190
3. Department of Physics, Columbia University, New York, NY 10027, USA

mengkun.liu@stonybrook.edu

db3056@columbia.edu

daiq@nanoctr.cn

CONTENTS

I. INTRODUCTION

Over the past decade, optical near-field techniques, especially scattering-type scanning near-field optical microscopy (s-SNOM), have undergone tremendous development. This is partly driven by the ever-increasing demand for the exploration of the nano-world and partly attributed to the many technical advances in laser and scanning probe technology. The wavelength independent spatial resolution of s-SNOM goes far beyond the Abbe diffraction limit [1], promising an explosive amount of applications that spread throughout the fields of physics [2–6], chemistry [7–12], biology [9,13–23], as well as various disciplines of engineering [24–30], geo- and space-related science [31]. The nature of the tip scattering and phase sensitive detection methods open up new opportunities in studying electromagnetic mode dispersion, light-matter interaction, and electron-lattice correlation with nanoscale resolution which conventional microscopy techniques, such as phase contrast microscopy [32,33], differential interference contrast microscopy [34], and laser scanning confocal microscopy [35], fail to achieve easily.

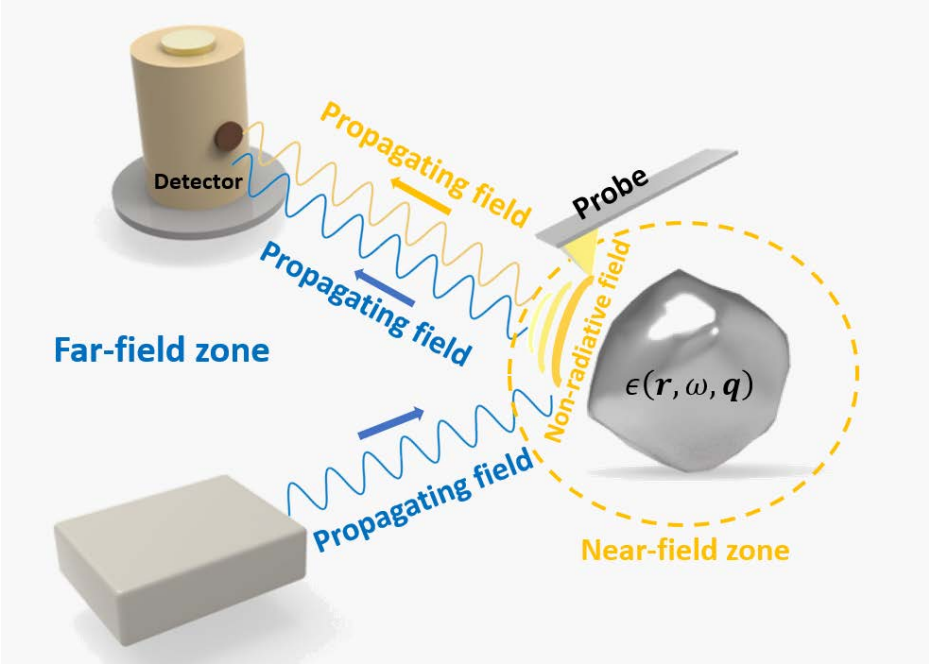

FIG 1. Far-field and Near-field measurements, accessing propagating field and evanescent field, respectively.

To conceptually elucidate the fundamental difference between a conventional 'far-field' optical measurement and a near-field measurement, one can imagine a simple scattering experiment of a macroscopic object as illustrated in **FIG.** 1. In general, the optical properties of this object can be characterized by the position- ($\boldsymbol{r}$), frequency- (ω), and momentum- ($\boldsymbol{q}$) dependent optical dielectric constant $\varepsilon(\boldsymbol{r},\omega,\boldsymbol{q})$. A light source far away

from the object generates propagating electromagnetic (EM) radiation (blue) which illuminates the object from free space. Upon illumination, the object induces two forms of EM field, namely the propagating field (blue) and the non-radiating field (yellow) [36]. The latter of the two decays exponentially normal to the sample surface. For infared illumination, the non-radiating field dies off typically within tens of nanometers, in the so-called near-field zone. The propagating field, on the contrary, can radiate into free space and be collected by a detector far away from the object. By analyzing the detected far-field signal, material characteristics such as its complex dielectric permittivity (or equivalently, complex optical conductivity or index of refaction) can be inferred based on classical EM theory. However, limited by diffraction, the focus size of the illumination is fundamentally prohibited to be much smaller than the wavelength. Consequently, the detected signal is insensitive to local variations of the object in a subwavelength length scale. More importantly, the information contained in the non-radiating near-field, which might encode important high spatial frequency (momemtum) properties of the object, is completely lost. The task of the near-field measurement is to retrieve the lost information with a spatial resolution not defined by free space optics. However, in order to achieve this several prices have to be paid. For one, a sharp probe shall be brought into the proximity of the sample surface and we are forced to handle a more complicated sample-probe ensemble instead of a much simpler isolated sample system. We also face the challenge to perfect our understanding of the optical properties of the probe, which can function as a light confiner (due to the extremely small radius of curvature of the apex) and a scatterer (partly due to its elongated shape, analogous to an antenna). Furthermore, the non-radiating field directly modifies the probe polarizability which eventually manifests itself into the detectable far-field scattered field (yellow) in a nontrivial way. With carefully excuted experiments and theoretical treatment, information of the object surface in a much smaller length scale can be gained. For more in-depth analysis and physical insights of the fundamental aspect of near-field optics, readers are directed to **ref** [37–39]**.**

s-SNOM is a scanning technique that encompasses these ideas. In this technique the sample is raster scanned under an oscillating AFM probe (commonly referred to as “the tip”) which serves as a nanoscale light confiner, enhancer, and scatterer. Compared to other scanning techniques such as scanning electron microscopy (SEM) [40], scanning tunneling microscopy (STM) [41], and scanning transmission electron microscopy (STEM) [42], s-SNOM offers very different dominant contrast. It yields optical properties (e.g. dielectric constant) beyond the diffraction limit with compatible spectroscopic capability and temporal sensitivity. At the same time, the AFM tip serves as a light momentum matcher which enables momentum ($\boldsymbol{q}$) resolved optical characterization typically on the order of $10\,nm^{-1}$ to $100\,nm^{-1}$, predominantly defined by the dimensions of the tip.

Like any other tip-based scanning techniques, it is not straightforward to understand the collected information due to nontrivial tip-sample interactions. For s-SNOM, these difficulties result from at least three factors. First, the well-known antenna effect [43] causes light to be highly confined between the probe apex and the sample surface. The specific geometry of the tip shank plays a significant role in determining the intensity of the scattered signal. Second, in addition to the local optical information, a strong but undesired background signal can be detected. This background signal can be mainly attributed to the light scattering from the tip shank, cantilever, and sample surface. Third, due to the broad momentum distribution of the localized radiation, in some cases nominally 'far-field trivial' phenomena such as nonlocality of the electrons and phonons need to be carefully addressed. These complications can occur in layer structures, thin films, plasmonic structures, and low-dimensional materials.

In this review article, we focus on the technical aspects of s-SNOM [44] which is also referred to as apertureless scanning near-field optical microscopy (ASNOM) or s-NSOM. **We discuss three key questions in great detail: How do different configurations of s-SNOM work? How do we understand the detected near-field signal? And what may be the next stage of the technical trend?** Previous reviews [45–50] of s-SNOM cover the technical progress from SNOM's first implementation in the 1970s to early 2000s and specific aspects such as infrared s-SNOM. Here we will only briefly introduce historical developments and we will maintain our main focus on the current stage and beyond. By reviewing publications within the recent decade, we will discuss the various probing techniques, signal demodulation methods, and progress in analytical and numerical methods for data interpretation.

II. HISTORICAL DEVELOPMENT

In 1928, Irish physicist Edward Synge proposed an idea of achieving optical resolution beyond diffraction limit [51] using an opaque metal film aperture with a small hole placed very close to the sample surface (as illustrated in **FIG. 2** (a)). He envisaged that when the size of the hole and the hole-sample distance is much smaller than the wavelength, sub-diffraction scattering through the hole can bring super-resolution. Realizing some technical difficulties in his original design, in 1932 he further proposed an alternative scheme in which he suggested to use a small object as the near-field optical probe (**FIG. 2** (b)) [52]. (O'Keefe [53] and Wessel [54] reinvented the aperture- and scattering-type schemes without knowing Synge's work latter on, respectively.) However, Synge's ideas were never experimentally realized at his time due to many technical challenges. For one, scanning techniques such as AFM were not implemented until the 1980s; For another, the nanotechnology was not as necessary as it is for today. Nevertheless, Synge's proposal certainly sparked the idea to practically implement super-resolution using near field.

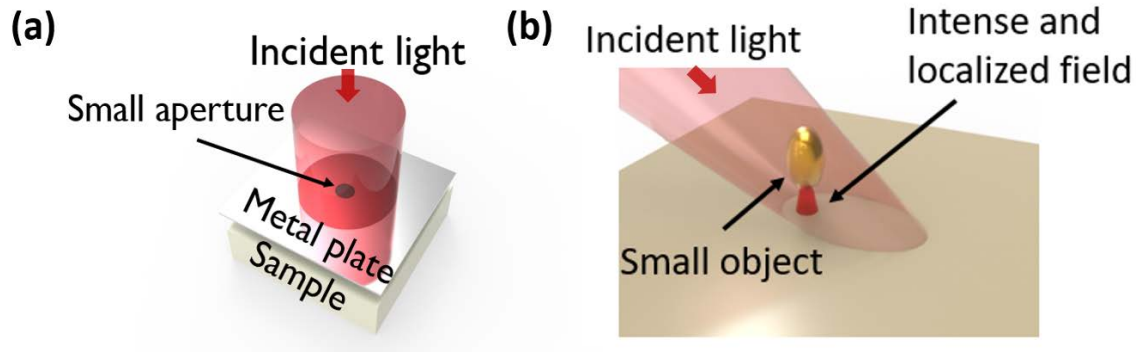

FIG 2. (a) Synge's original idea of overcoming the diffraction limit and achieving ultrahigh spatial resolution using a small aperture. (b) Synge's second idea with a small subwavelength object as light confiner and scatterer.

In the late 1970s and early 1980s, progress in scanning probe technologies with sub-nanometer precision [55] eventually led to the experimental fruition of Synge's ideas [56–61]. In a 1986 study by the Nobel laureate Betzig and colleagues [58], a line scan across an aluminum grating was performed to yield ~150 nm resolution with incident wavelength ~500 nm (**FIG. 3** (a)). (As a side note: readers are encouraged to read Betzig's Nobel lecture [62], in which he eloquently summaries the quest for sub-diffraction resolution from the 1980s to the late 2000s. Likewise, his work detailing the concept of near-field optics is still insightful for today's audience [59].) In a 2000 study by Hecht *et al.* [63], the measurement of a metal island film achieved a resolution of $\lambda/10$ (~50 nm resolution with 633 nm incident) (**FIG. 3** (b)). In both studies, optical contrasts between different materials were clearly observed. Different from the scattering-type near-field systems, near-field instruments in the early days usually employed an aperture probe which functioned as a waveguide and sub-diffraction emitter [63], similar to the original scheme Synge proposed. Today, aperture-based SNOM is still a popular technique offering unique advantages especially with visible or ultraviolet illumination [64–81]. A detailed review on aperture based SNOM can be found in **ref** [63]. In principle, aperture SNOM can achieve very high resolution by making the aperture size arbitrarily small. However, in practice the resolution is limited to approximately $\lambda/10$ due to the waveguide cut-off effect [44]. This means for mid-infrared (mid-IR) light the resolution is on the order of few hundred nm to 1 μm, which in many cases does not meet the desired nanoscale criterion. In the case of THz illumination, the resolution is on the order of tens of microns [82] where practical applications in nanoscience become difficult to achieve.

Intense efforts devoted to developing s-SNOM occurred in the late 1990s. One of these pioneering s-SNOM imaging works was published by Lahrech *et al.* in 1996 [83]. In their work, they performed s-SNOM imaging of a gold grating and gold surface (**FIG. 3** (c) and (d)) and observed clear optical contrasts with an impressive sub $\lambda/100$ resolution.

Contrastingly from aperture based SNOM, modern s-SNOM typically illuminates a metalized AFM probe with a focused laser beam at an oblique angle of incidence. The achievable resolution of s-SNOM is practically only limited by the radius of curvature of the tip apex. The metal coated tips are usually based on Si cantilevers which are commercially available and economical.

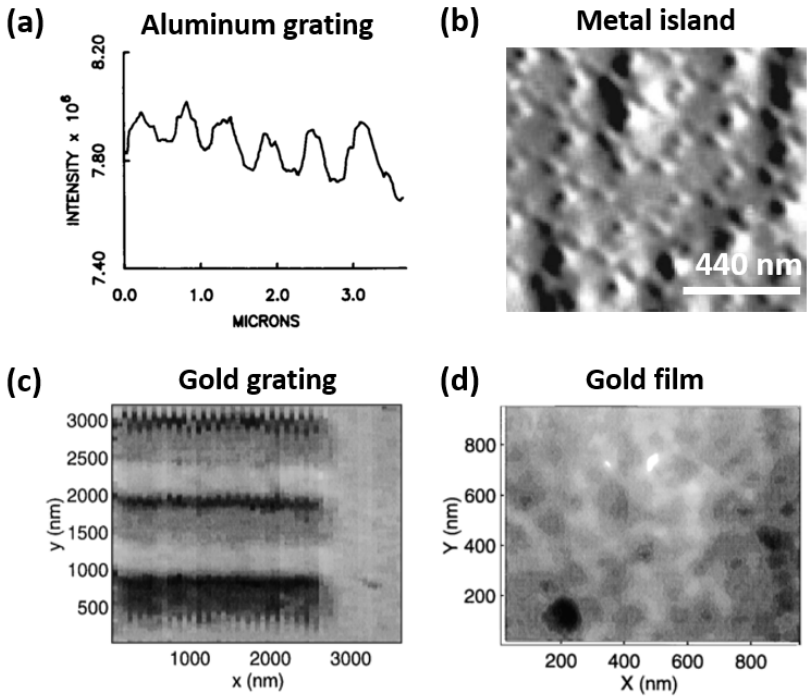

FIG 3. Representative measurement results from early studies using near-field techniques. (a) A line scan across an aluminum grating with ~500 nm visible illumination. (b) Imaging of a metal island film with 633 nm visible illumination. (c) Imaging of a gold grating and (d) imaging of a gold film surface with 10.6 μm infrared illumination. (a) and (b) are aperture SNOM measurements. (c) and (d) are s-SNOM measurements.

III. CURRENT STAGE

The most commonly used contemporary s-SNOM systems are at the visible and IR frequency ranges using continuous-wave (CW) light sources. Thanks to the development of highly stable commercial lasers such as gaseous, fiber-based, and quantum cascade lasers (QCLs), typical laser noise can reach below $100\ nV/\sqrt{Hz}$ at $\sim 100\ kHz$. The result is a promisingly good signal to noise ratio (SNR) for near-field detection. This SNR has been a critical development for s-SNOM because laser noise is usually the largest limiting factor for sensitive optical measurements. The noise of state-of-the-art IR detectors is typically below $\sim 30\ nV/\sqrt{Hz}$. In addition to CW lasers, ultra-broadband or tunable light

sources, including synchrotron IR radiation and ultrafast fiber or solid state lasers, have been successfully demonstrated to be useful for s-SNOM. These sources offer additional temporal and spectral resolution. The synchrotron source produces about 1 microwatt per wavenumber upon a diffraction-limited spot. The result is roughly 1 mW over a 1000 cm^{-1} wide spectral range. This is orders of magnitude higher than blackbody radiation sources.

While s-SNOM is still a nascent field, it has a large potential to bring new physics into the experimental scope including nonlocal effects. This is especially true at longer wavelengths (e.g. at THz frequency) since the light is tightly confined. The nonlocal electron transport starts to contribute significantly to the near-field-accessible sample volume under the tip. Additionally, operating s-SNOM at cryogenic temperature or in a gaseous environment may aid the quest for low energy quantum phenomena. By coupling this with other imaging techniques, such as focused X-ray diffraction (nano-XRD) and Raman spectroscopy, s-SNOM can yield a multi-degree characterization of electrons, phonons, and magnetization. In the following sections we will start with the basics and introduce these new branches of s-SNOM in greater detail. We will restrain ourselves to the discussion of references mainly within the recent decade (mostly around or after the year 2010) to cover the latest progress in this field.

A. Prevailing near-field techniques and examples of experimental accomplishments

1. s-SNOM with CW sources

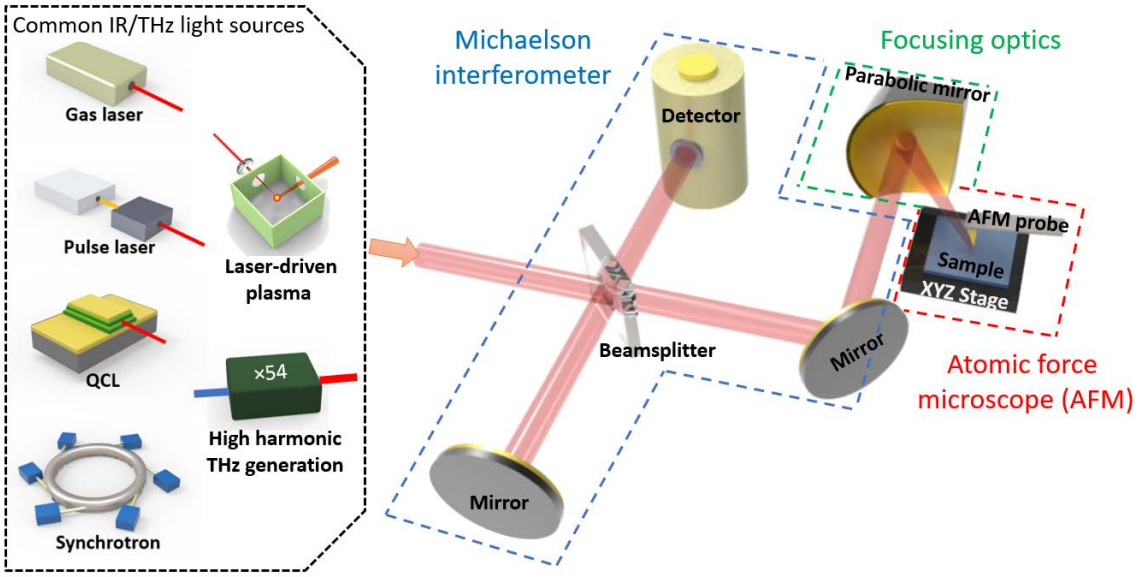

FIG 4. A typical s-SNOM setup with visible or IR light sources.

s-SNOM imaging is best when equipped with a monochromatic CW source [84,85]. Most CW lasers at IR range are capable of providing a high output power of up to hundreds of mW and maintain a high level of stability over long periods of time. For example, the hour power fluctuation of a typical CO_2 laser is usually below 1%. A He-Ne laser can perform much better, down to 0.1%. The high power-stability and low RMS noise are crucial for performing long-time raster scans for high-resolution images.

A typical visible/ IR s-SNOM setup can be found in **FIG. 4**. The incident light is divided by a beamsplitter into a reference arm and a probing arm. The probing beam is focused (within the diffraction limit) by focusing optics, typically a parabolic mirror or a lens, onto the apex of the AFM tip. Light interacts with the tip-sample system and gets scattered elastically. The backscattered (or in some cases forward scattered) light follows the same (or different) beam path back to the beam splitter and eventually gets collected by the detector. The reference beam is reflected from a flat mirror on a delay stage and interferes with the backscattered light at the detector. The result is the formation of an asymmetric Michaelson interferometer. This allows one to access both amplitude and phase information of the scattered light, yielding the possibility of extracting local complex dielectric functions of the sample volume under the tip, without invoking the Kramers-Kronig relations.

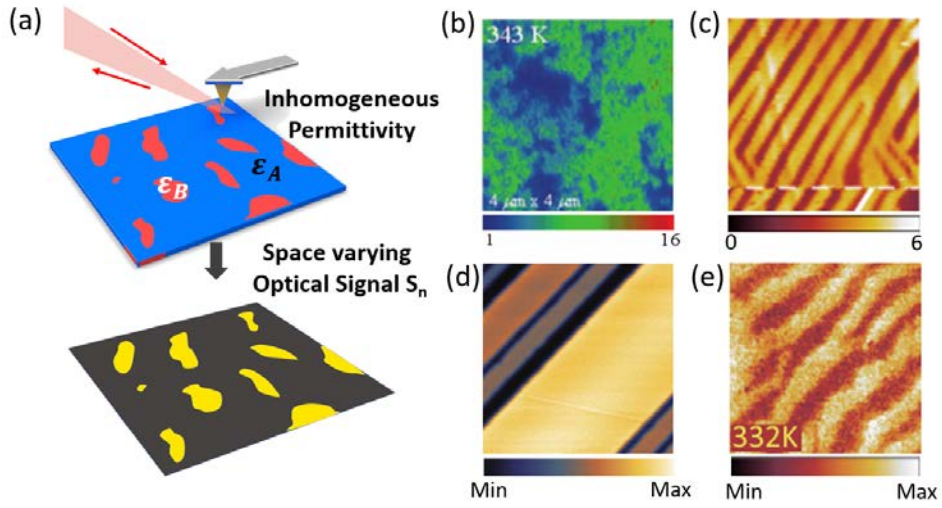

FIG 5. (a) Schematic demonstration of s-SNOM mapping of the local sample permittivity due to phase separation at the nanoscale. (b)-(e) Different phase inhomogeneity patterns observed on near-field amplitude images during temperature-induced IMT phase transition process on VO_2 films grown on different substrates. (b) VO_2 on sapphire substrate. (c) VO_2 on $[100]_R$ TiO_2. (d) VO_2 on $[110]_R$ TiO_2. (e) VO_2 on $[001]_R$ TiO_2.

With CW visible/ IR s-SNOM, a wide range of canonical systems have been intensely investigated. Major categories in a condensed matter system include, but are not limited

to: mesoscopic phase inhomogeneity in strongly correlated quantum materials [3,30,86–101], polaritonic wave propagation in plasmonic or dielectric samples, especially low-dimensional materials like graphene and boron nitride [6,102–129], and subwavelength electrodynamic responses from artificial nanostructures [4,5,27,28,94,106,130–152].

In strongly correlated electron materials (SCEM) [99,153,154] s-SNOM was first employed to study phase separations in transition metal oxides. Since most of the SCEM systems are composed of "bad metals" and "bad insulators", the optical contrast in a typical near-field image faithfully represents the variations in sample permittivity **FIG. 5** (a). In a landmark 2007 study by Qazibash *et al.*, the temperature induced insulator-metal transition (IMT) in vanadium dioxide (VO_2) was directly imaged with IR s-SNOM (**FIG. 5** (b)) [3]. Due to the inhomogeneity in local dielectric permittivity during the IMT, local scattering amplitude exhibited distinct contrast. In later studies, unidirectional phase separations were observed in epitaxial VO_2 films grown on TiO_2 substrate with different crystal orientations [96,98,100]. Due to the distinct strain environment, a variety of pattern formations at elevated temperatures were directly imaged (**FIG. 5** (c), (d), and (e)). It becomes relatively easy to study SCEM with s-SNOM compared to other techniques due to its larger scanning area (up to 100 μm by 100 μm) and wider working temperature range (up to 450K). A detailed review on this subject can be referred to the review article by Liu et al [99].

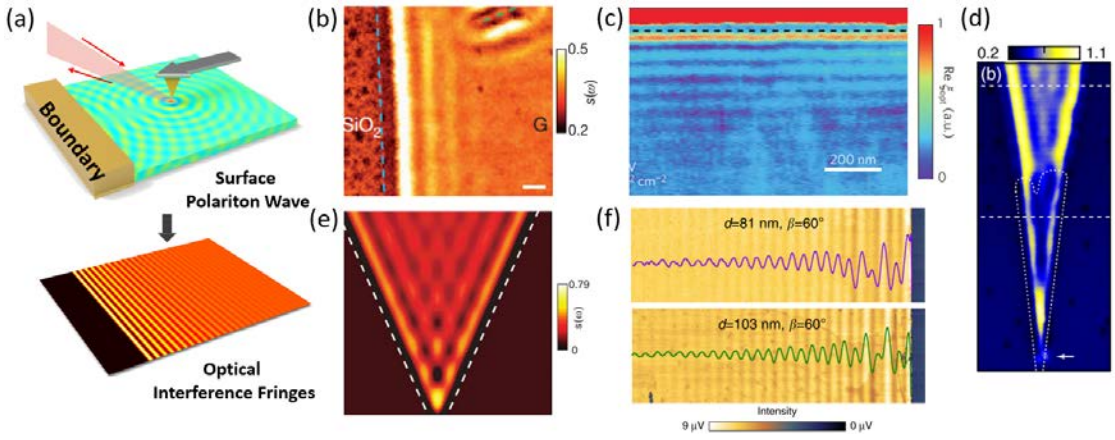

FIG 6. (a) Schematics demonstrating s-SNOM direct imaging of the interference patterns due to propagating polaritonic waves. (b), (c), and (d) Interference of graphene surface plasmons. (e) Interference pattern of hBN surface phonon polaritons. (f) Interference pattern of MoS_2 waveguide mode.

Additionally, s-SNOM accesses a broad range of in-plane momentum due to the light-tip interaction. This property has enabled the direct visualization of surface polaritonic wave propagation, e.g. surface phonon-polaritons or plasmon-polaritons. In most cases, the AFM tip scatters the incident light and launches a cylindrical polariton wave of wavelength

λ_p. This tip launched polariton wave can interfere with the boundary-reflected wave (**FIG. 6** (a)) and form a periodic standing wave pattern of wavelength $\lambda_p/2$. Representative studies by Fei *et al.*, Woessner *et al.,* and Gerber *et al.* demonstrate the interference patterns of graphene plasmons in **FIG. 6** (b), (c) and (d), respectively [5,103,104]. In a 2014 study by Dai *et al.,* interference patterns of surface phonon polaritons on a hexagonal boron nitride (hBN) were reported (**FIG. 6** (e)) [6]. Recently, Hu *et al* obtained the interference pattern of waveguide modes to infer the anisotropic dielectric function of MoS_2 (**FIG. 6** (f)).

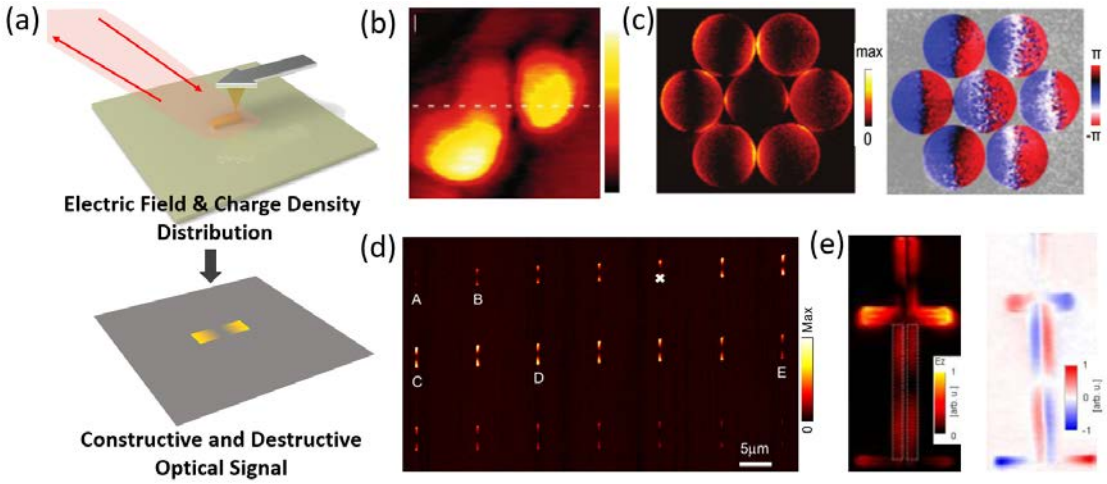

FIG 7. (a) Schematics of s-SNOM imaging of plasmonic nanostructures. (b) Imaging of resonant gold nanoparticles. (c) Imaging of structure disk array. (d) Investigation of dipolar antennas with different lengths. (e) Imaging of a folded dipole antenna. The yellow and black color scheme represents the near-field amplitude while the blue and red color scheme represent phase images.

Another heavily investigated application of s-SNOM is the study of plasmonic nanostructures and metamaterials below the unit cell scale. The sample units are usually an order of magnitude smaller than the wavelength of interest. Due to the high sensitivity to local electric field and charge accumulation, s-SNOM is an ideal tool to visualize the field and charge distribution induced in plasmonic nanostructures (**FIG. 7** (a)). For instance, a pioneering study in 2001 by Hillenbrand *et al.* used s-SNOM to study the plasmonic resonance of gold nanoparticles (**FIG. 7** (b)) [134]. Research interest in this topic has no sign of slowing down within the decade. Here we present results from four representative studies by Alonso-Gonzalez *et al.* and Xu *et al.* where nano-disks, bars, and antennas are studied (**FIG. 7** (c) (d) (e)) [132,135,138]. Conventionally, spatial mapping of

nanostructure resonances can be indirectly studied by numerical simulations or by far-field measurements. With s-SNOM different resonance modes are neatly visualized.

Other notable applications of CW visible/ IR s-SNOM include studies of the nonlinear and thermal effects in the near-field [155], characterization of sample thickness and optical constants [156–160], enhancing signal by manipulating sample environment [161,162], and so on. Govyadinov *et al.* demonstrated in their 2014 study that sample thickness and permittivity can be simultaneously and quantitatively extracted from s-SNOM images demodulated at multiple harmonics of the tip oscillation frequency [156]. In the following year, Wang *et al.* showed that not only was it possible to map the conventional lateral near-field interaction, but also the vertical near-field response, i.e. the near-field confinement in the direction normal to sample surface. This provides the ability to map a full three-dimensional near-field interaction between the tip and the sample [163,164].

2. s-SNOM in time domain

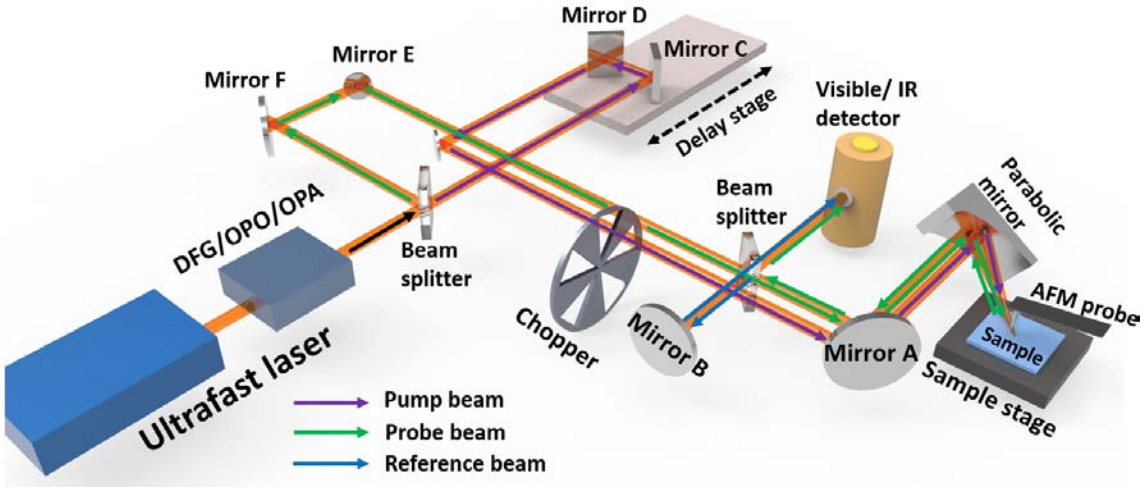

FIG 8. Example of an ultrafast near-field pump-probe spectroscopy setup.

Ultrafast optics has been widely employed to investigate dynamics of carriers including electrons, spin, and phonons at femtosecond (fs) and picosecond (ps) time scales [165,166]. The s-SNOM setup is compatible with conventional pump-probe techniques where a great variety of experimental schemes exist depending on the specific needs [167]. An example of an ultrafast pump-probe near-field setup is shown in **FIG. 8**.

Ultrafast s-SNOM was pioneered by Wagner *et al*. in 2014 with two seminal works on InAs and exfoliated graphene [168,169]. By analyzing the area dependent near-field signal evolution at ~100 fs scale they were able to reveal the enhanced plasmonic response. This response was attributed to the effective electron temperature increase following the

photoexcitation (**FIG. 9** (a)). Subsequent studies by O'Callahan *et al.* and Donges *et al.* used ultrafast IMT dynamics to investigate VO_2 nanocrystals with optical-pump/ optical-probe and optical-pump/ IR-probe setups (**FIG. 9** (b) and (c)), respectively [170,171]. In a 2014 study by Eisele et al., IR-pump/ THz probe measurements of an InAs nanowire uncovered its photoinduced carrier dynamics at a range of 30 - 40 THz (**FIG.** 9(d)). In a 2016 study by Ni et al., an IR-pump/ IR-probe experiment on graphene neatly mapped out the time-dependent plasmon-polariton dispersion and revealed the time-dependent photodoping effect with momentum resolution (**FIG.** 9 (e)).

An ambitious goal of this nascent research with ultrafast s-SNOM is to study photo-induced dynamics without the limitation of sample size, which brings nanoconfinement and plasmonic imaging into the central stage. Despite the early successes, many problems remain to be solved. For example, laser repetition rate has to be in an appropriate range. It can not be too high—pulse energy too small. It can not be too low either—low yield in the signal detection. In addition, the high pulse power can induce accumulative heating in the tip and result in unstable AFM operation. Future development of ultrafast s-SNOM with a repetition rate in the range of a few hundred kHz can be a good compromise [172].

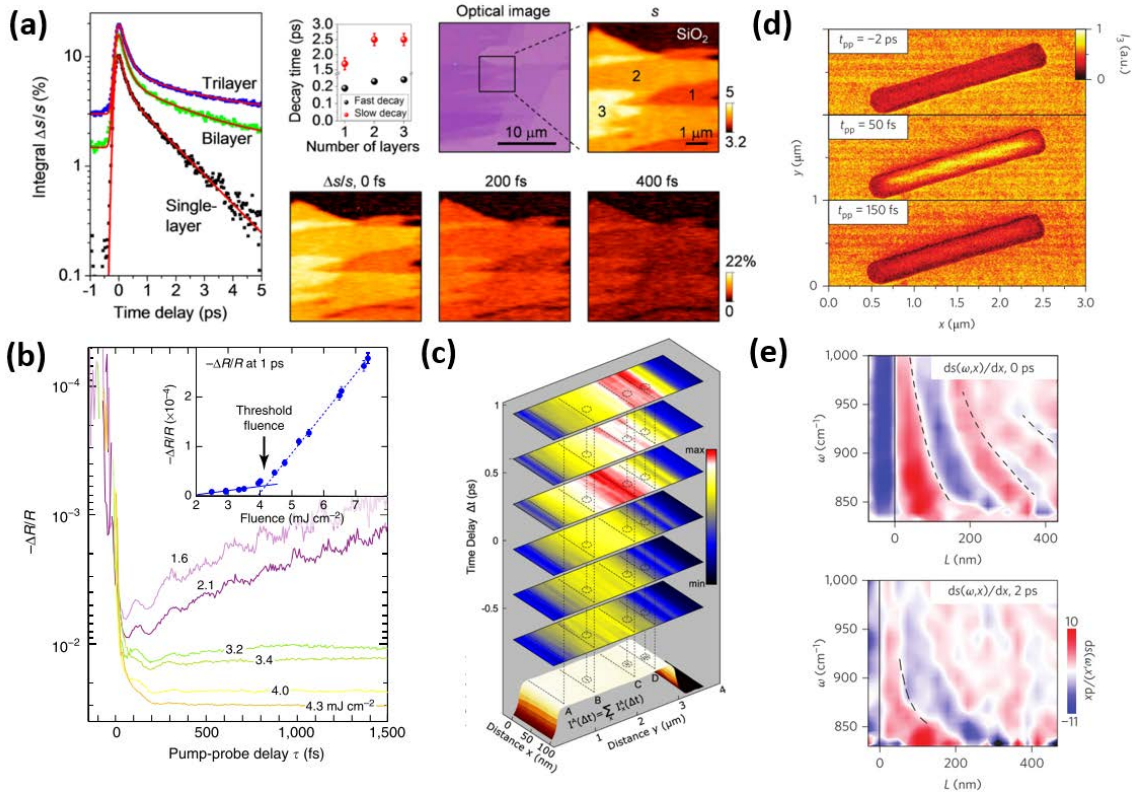

FIG 9. Representative ultrafast s-SNOM studies. (a) Optical pump/ optical probe s-SNOM of graphene. Results show a layer dependent near-field signal decay. (b) Optical pump/ optical near-field probe of VO_2 nanocrystals. Result shows the transient near-field reflectivity with different pump fluences. (c) Optical pump/ optical probe s-SNOM

of VO_2 nanocrystals. Result shows spatiotemporal images of photoinduced insulator to metal transition. (d) IR-pump/ THz probe s-SNOM of an InAs nanowire reveals ultrafast photoinduced carrier dynamics. (e) IR-pump/ IR-probe s-SNOM of graphene maps out time-dependent plasmon-polariton dispersion.

3. s-SNOM for broadband nano-spectroscopy

Monochromatic illumination produces superior image quality by utilizing the fine linewidth and high power (watt per wavenumber) of CW lasers. Broadband spectroscopy, on the other hand, can deliver point-by-point spectral information with a much broader bandwidth (200 cm^{-1} to 2000 cm^{-1}). The idea of combining spectral measurement to s-SNOM gained recognized popularity in the late 2000s and early 2010s [10,19,21–23,27,31,128,150,152,173–181] along with the development of intense and high repetition rate tunable-QCLs and ultrafast fiber-based amplifiers. Synchrotron light sources have also been explored as ultra-broadband sources for s-SNOM. Based on Fourier-transform infrared spectroscopy (FTIR) techniques that are well established for far-field optics, IR spectroscopy with 10 to 20 nm resolution can be routinely achieved.

The reference arm differentiates broadband and monochromatic s-SNOM (**FIG. 4**). In a broadband s-SNOM experiment, the reference mirror scans over a wider spatial range so that an interferogram (detected light intensity versus optical path difference) is obtained. The complex-valued near-field spectrum is calculated by imposing Fourier transform on the near-field interferogram. On the other hand, with a tunable laser system the experiment decomposes into multiple steps of CW s-SNOM measurements without the interferogram.

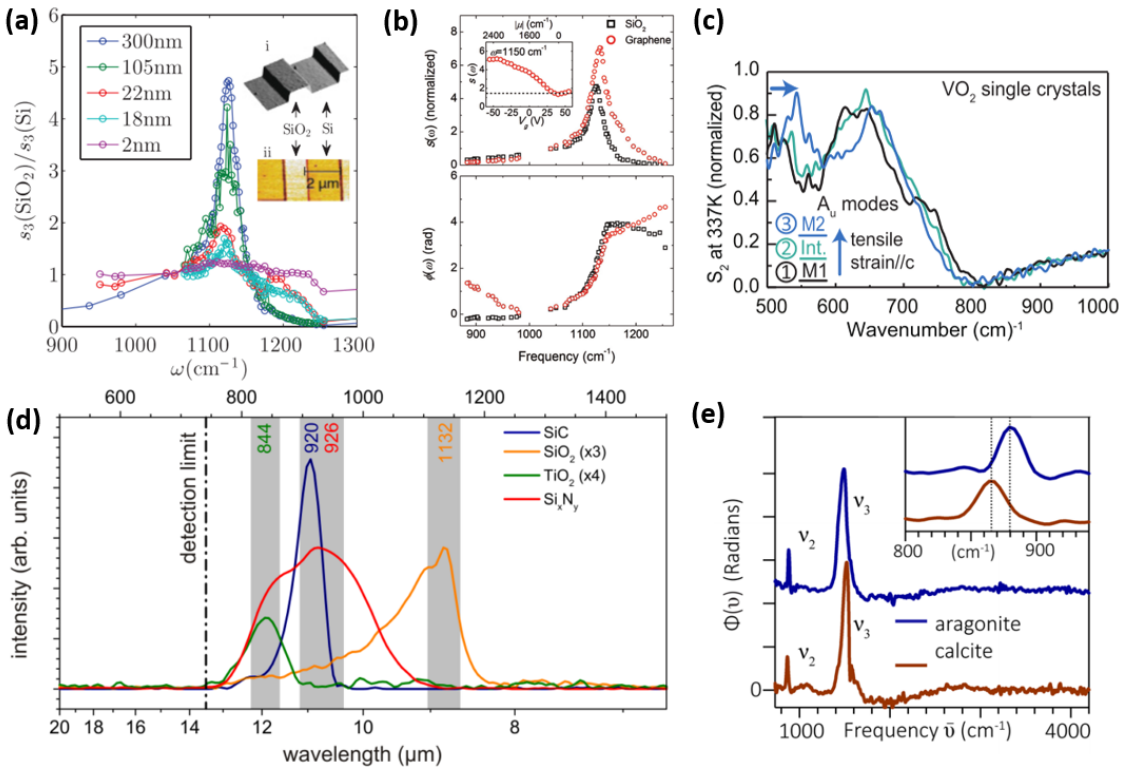

FIG 10. Examples of near-field spectroscopy measurements. (a) Near-field spectrum of SiO_2 films with different thickness. (b) Near-field spectrum of graphene on SiO_2. (c) Location dependent near-field spectrum of single crystal VO_2 at room temperature. (d) Near-field spectrum of four common semiconductors. (e) Near-field spectrum of mollusk shells at two different stages as aragonite and calcite.

Some noticeable examples of broadband nano-IR experiments are as follows. In a 2012 study by Zhang *et al.*, SiO_2 thin films with different thickness on a Si substrate were studied in the frequency domain to assess the accuracy of two different theoretical models. With a combination of CO_2 lasers and QCLs they successfully mapped out the spectrum of SiO_2 phonons in the frequency range from 900 cm^{-1} to 1300 cm^{-1} (**FIG. 10** (a)) [182]. In comparison to the theoretical calculation, they demonstrated the importance of accounting for the length of the tip shank in theoretical models. In a 2011 study by Fei *et al.*, the hybridization of graphene plasmons and SiO_2 surface phonons were investigated thoroughly with a similar s-SNOM spectroscopy technique (**FIG. 10** (b)). In a 2014 study by Wagner *et al.*, an IR ultrafast laser was employed as a source for broadband s-SNOM measurement [168]. Broadband investigation of SCEM has also been demonstrated to infer the correlation between the electron and lattice during a nanoscale insulator to metal phase transition. For example, Liu *et al*. in their 2015 work revealed two different IR active monoclinic phonon modes (M1, M2) at adjacent locations (subwavelength) on the surface of a single crystal VO_2 sample (**FIG. 10** (c)) [100]. Hermann *et al.,* in their 2014 study characterized the distinct near-field responses of different semiconductors with a

broadband synchrotron light source (**FIG. 10** (d)) [183]. Muller *et al.* demonstrated the capability of chemical fingerprint identification of mollusk shells with different compositions (**FIG. 10** (e)) [10].

Although spectroscopy can be performed with tunable lasers or pulsed lasers, the synchrotron light source (SLS) usually offers a broader simultaneous bandwidth which can greatly enhance the experimental throughput of s-SNOM. SLS can produce about 1 microwatt per wavenumber into a diffraction-limited spot. The result is about 1 mW over a 1000 cm^{-1} spectral range which satisfies the minimum requirement for s-SNOM detection. There are a number of synchrotron sites that provide IR near-field spectroscopy (nano-FTIR) facilities including Advanced Light Source (ALS) SINS beamline in Lawrence Berkeley Laboratory (LBL), Berkeley, California, USA; Metrology Light Source (MLS) in Germany; Laboratório Nacional de Luz Sincrotron (LNLS) in Brazil; ElectroMagnetic Infrared Radiation (EMIRA) in Jordan, and the SPring-8 synchrotron site in Japan [184–189]. They can routinely perform IR s-SNOM spectroscopy (also known as nano-FTIR or broadband nano-IR) measurements from below 600 cm^{-1} to 2500 cm^{-1} (4 to 15 μm) with reliable SNR and below ~8 cm^{-1} spectra resolution [8]. New possibilities also exist in other national facilties such as NSLS-II at Brookhaven National Laboratory (BNL), which can in principle provide 2 to 100 μm wavelength bandwidth with new generation of stable synchrotron IR light sources. Other noticeable techniques include the use of high-temperature plasma generated in a gaseous environment as a broadband table-top light source. An impressive bandwidth and reasonable SNR has been demonstrated recently [190,191].

B. Emerging techniques and cutting-edge experiments

1. s-SNOM towards longer wavelengths

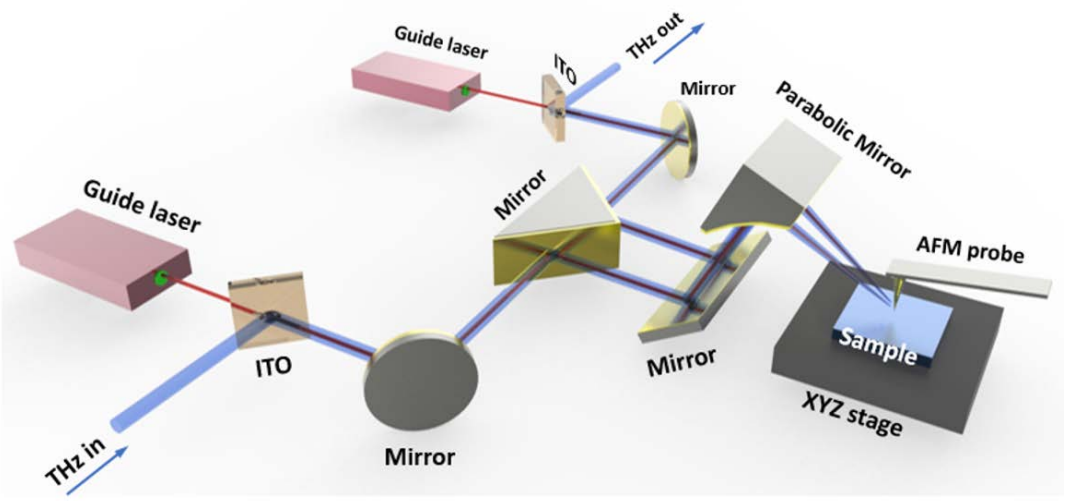

FIG 11. An example of a THz s-SNOM setup.

Operating s-SNOM at the far-IR and THz frequency range deserves its own chapter due to the many technical difficulties it encounters. As the 'THz gap' (a lack of an intense source from 0.1 to 10 THz) has been gradually filled in the far-field, near-field THz-SNOM meets an even more stringent requirement. Of course, challenges and efforts do not come without reward. Due to its low photon energy, THz is ideal for non-invasive diagnosis of biological substances [192–195] and probing many low energy excitations in quantum systems including phonons, cyclotron, and the energy gap in high-temperature superconductors and quantum wells [196]. Accessing the near-field regime allows for many applications in condensed matter and biophysics, especially combined with cryogenic conditions as we will detail in the next session.

Historically, attempts to generate THz radiation were first carried out by using frequency mixing [197], QCLs [198–200], and free electron lasers. The first set of scattering-based THz near-field experiments were developed in the mid-2000s [201–204]. Later on, THz waveguide probes were successfully demonstrated in the early 2010s [205,206]. Higher harmonic signals ($n \geq 2$) were experimentally obtained first in 2008 by Huber *et al.* They used a CW CH_3OH gas laser operating at 2.54 THz to image a Si transistor and demonstrated the quantitative characterization of local carrier concentration and mobility with nanometer resolution (**FIG. 12** (a) [26]). In the same year, Ribbeck *et al.* successfully demonstrated the THz s-SNOM measurement of Si with different doping levels [207]. Jacob et al in 2012 used a free electron laser to perform THz s-SNOM imaging of InAs quantum dots and successfully observed contrast induced by transitions between two confined states belonging to the same band [164]. At the time of these studies, radiation generated by gaseous lasers and THz QCLs suffered from low emission power or narrow bandwidth which limited the SNR and spectroscopic applications. THz generated from nonlinear crystals (ZnTe) or the photo-Dember effect (InAs) can in principle yield higher instantaneous power (pulse energy) and good bandwidth [207,209,210]. However, due to the low repetition rate usually used for pump excitation (e.g. 1 to 10 kHz), a decent SNR in near-field will require unbearable long acquisition time. A high repetition rate, high SNR THz source must be used. In this case, the photoconductive antennas (PCA) have been proven to be useful. The PCA was introduced in the late 1980s and early 1990s [211,212] providing a dynamic range reaching above 80 dB at the 0.2 to 3 THz frequency range. The state-of-the-art PCAs can generate ultrashort pulses with a frequency range of up to 15 THz [213]. With further improvement one can envisage that the PCAs can be a dominant tool for broadband THz s-SNOM [214].

A typical PCA based THz s-SNOM setup is shown in **FIG. 11**. In order to maximize the THz signal, the incident and scattered light are separated into two different beam paths by removing the beam splitter (of course, this scheme is suitable for IR as well). In practice, two visible guide lasers are often used for easy alignment of the THz beam. Indium tin oxide (ITO) works well as a THz mirror, but partially transmits the guide beam. This serves as an ideal dichroic beam splitter for THz and visible light. Since lenses are often avoided

for diffraction-limited focusing at THz frequencies, parabolic mirrors are required. The scattered light is collected on the other side and detected at the PCA receiver.

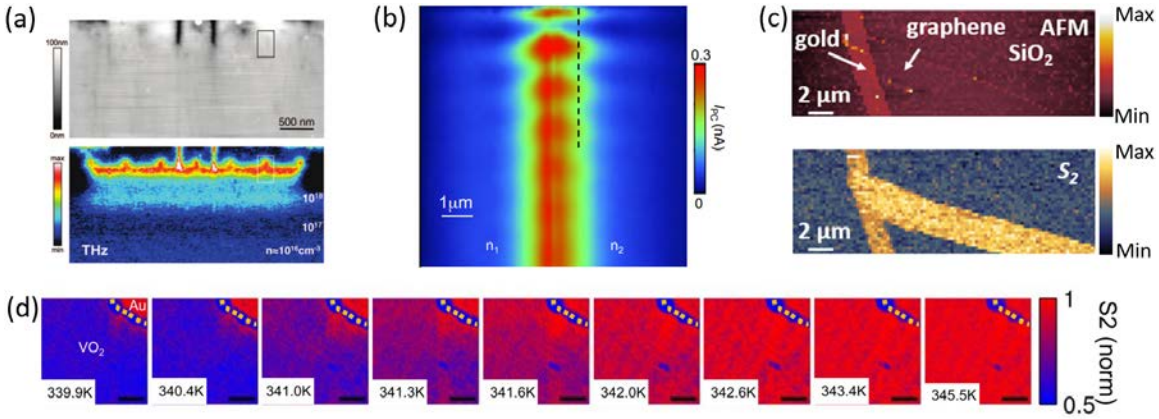

FIG 12. Representative THz s-SNOM studies. (a) Top: AFM topography image. THz s-SNOM imaging of a transistor device with a gas laser operating at 2.54 THz. Carrier concentration and mobility can be quantitatively identified. (b) THz photocurrent imaging of slow plasmons in a split-gate graphene photodetector. (c) THz s-SNOM imaging of graphene monolayer with a gold reference and PCA-generated broadband THz illumination. (d) THz s-SNOM of IMT of VO_2 with a PCA-generated broadband THz illumination.

Despite THz s-SNOM's adolescence, successful experiments in the field have been performed with regularity in recent years. Moon *et al.* presented a THz s-SNOM imaging study of a gold grating under a Si_3N_4 layer in 2015 [215]. Stinson *et al.* reported a direct observation of IMT of VO_2 with THz s-SNOM (**FIG**. **12** (d)) in 2018 [ref after published?]. In the same year Zhang *et al* observed high near-field reflectivity of a graphene monolayer (**FIG. 12** (c)) with a near-field signal comparable to the noble metals. [ref after published]. Another 2018 study by Liewald *et al* proposed an electronics-based s-SNOM setup operating from 0.5 to 0.75 THz by high-harmonic generation of microwaves [216]. In addition to the ever-seeking battle for better THz sources, recent studies have found various ways to overcome the low scattering signals and make equally scientific important, but more amenable, schemes. For example, in a 2016 study by Alonso-Gonzalez *et al.* and a 2017 study by Lundeberg *et al*., THz graphene plasmons were mapped with near-field photocurrent generation (**FIG. 12** (b)) [217,218]. In a 2017 study by Klarskov et al. [219], a THz emission microscopy scheme is proposed where IR incident beam interacts with the tip-sample system and terahertz emission due to nonlinear response is detected in the far-field. Low repetition rate and high-power THz generation via ZnTe, $LiNbO_3$ or InAs can in principle be used in the near-field THz-photocurrent and THz emission scenarios since they yield much higher SNR. We anticipate this field will be a new research frontier with exciting physics to come in the following years.

2. s-SNOM at low temperature and high magnetic field

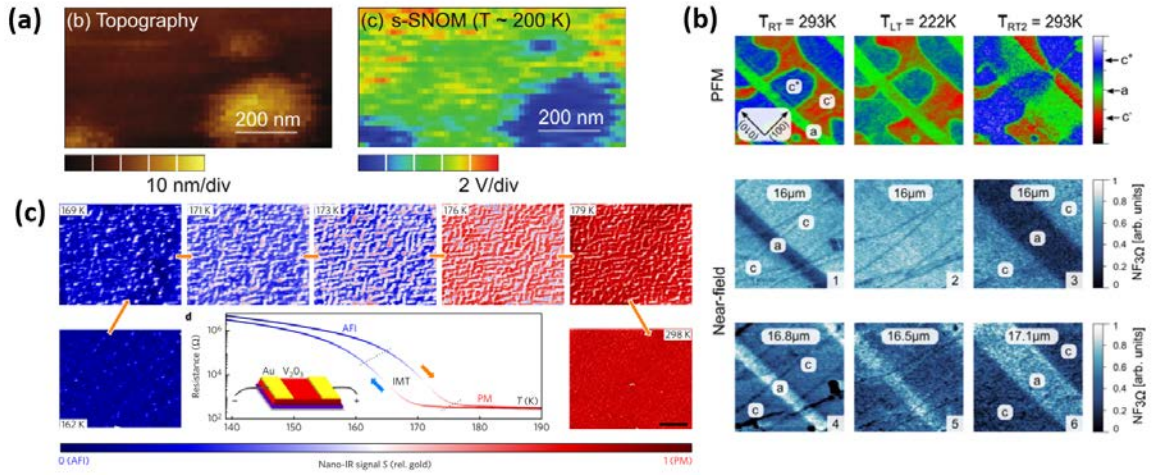

FIG 13. Representative low-temperature s-SNOM studies. (a) s-SNOM imaging of V2O3 IMT at ~200 K. (b) s-SNOM imaging of ferroelectric domains at ~222 K and room temperature. (c) s-SNOM imaging of V2O3 IMT from 169 K to room temperature.

A daunting quest in the field of s-SNOM is to perform routine measurements at cryogenic temperature, namely cryo-s-SNOM. Although its importance is universally recognized, cryo-SNOM is technically challenging for a number of reasons. To start, conventional AFM cannot work in high vacuum and low temperature environments. It requires nine positioners (three for the sample, three for the focusing mirror, and three for the tip) that work independently. Furthermore, it requires a cryo-scanner with a reasonably large travel range (since s-SNOM operates at a much larger scanning range than STM) and good radiation shielding to compensate for the thermal loss which originates from various optical components. The first study on low-temperature s-SNOM was from Yang *et al* in which s-SNOM images of V_2O_3 during IMT at ~200 K were performed (**FIG. 13** (a)) [220]. In the following year, Döring *et al* demonstrated s-SNOM imaging of BTO ferroelectric domains at ~222 K (**FIG. 13** (b)) [86]. In 2016, McLeod *et al* systematically demonstrated the use of s-SNOM to study SCEM by observing IMT of V_2O_3 at 160-180 K with extremely high spatial resolution and SNR (**FIG. 13** (c)) [2]. Very recently, Ni *et al.* explored the fundamental limits to graphene plasmonics with cryo-s-SNOM operating at 60 K, observing long-distance plasmon propogation [221].

As cryogenic environments and magnetic excitation often come hand in hand, operating s-SNOM with a strong magnetic field present is another new and exciting research focus. So far the experimental results have only been demonstrated with scanning microwave impedance microscopy (sMIM) [222–225] which relies on electronic instead of optical

scanning techniques. Magneto optical imaging with the near-field technique has been demonstrated but still awaits more further exploration [226–228].

3. s-SNOM and its integration with other techniques

Inherently, the s-SNOM apparatus bridges far-field electromagnetic propagation and microscopic (near-field) scanning methods. Therefore, this versatile platform can be integrated into many other optical and non-optical techniques. For example, surface-enhanced Raman spectroscopy (SERS) has gained tremendous popularity over the past couple of decades due to its fine sensitivity to molecular vibrations and absorptions [229–231]. The concept of combining SERS and s-SNOM has been successfully achieved [232].

Focused X-ray diffraction (nano-XRD) is an important tool for crystallography research with enhanced spatial resolution, typically within micron scale. Nano-XRD achieves high resolution by focusing X-rays with a Fresnel zone plate or a Kirpatrick-Baez mirror [233,234]. This state-of-the-art nano-XRD experiment currently can probe a resolution of 30 nm, comparable to s-SNOM resolution. It's well known that XRD experiments reveal crystal lattice information. Combining nano-XRD to s-SNOM conveniently investigates a sample's optical and structural properties concurrently at the nanometer scale. The first of its kind is currently under development at the Advanced Photon Source (APS) in Argonne National Laboratory (ANL).

Another potential combination is the integration of s-SNOM with scanning thermal microscopy (SThM). SThM measures a sample's thermal properties such as surface temperature and thermal conductivity. The feasible resolution for commercially available products is also close to 50 nm. Coupled with s-SNOM, optical and thermal properties can be simultaneously measured. In addition, ultrafast THz STM can be combined with THz cryo-s-SNOM since they share the same essential optics and hardware.

At the end of this session, we show a few tangible imaging systems: cryo-SNOM (**FIG. 14** (a)), synchrotron-based broadband s-SNOM (**FIG. 14** (b)) and nano-XRD + s-SNOM systems (**FIG. 14** (c)). The complexity of s-SNOM requires a careful examination of the theory and understanding of the acquired signals, as we will discuss in the next two sections.

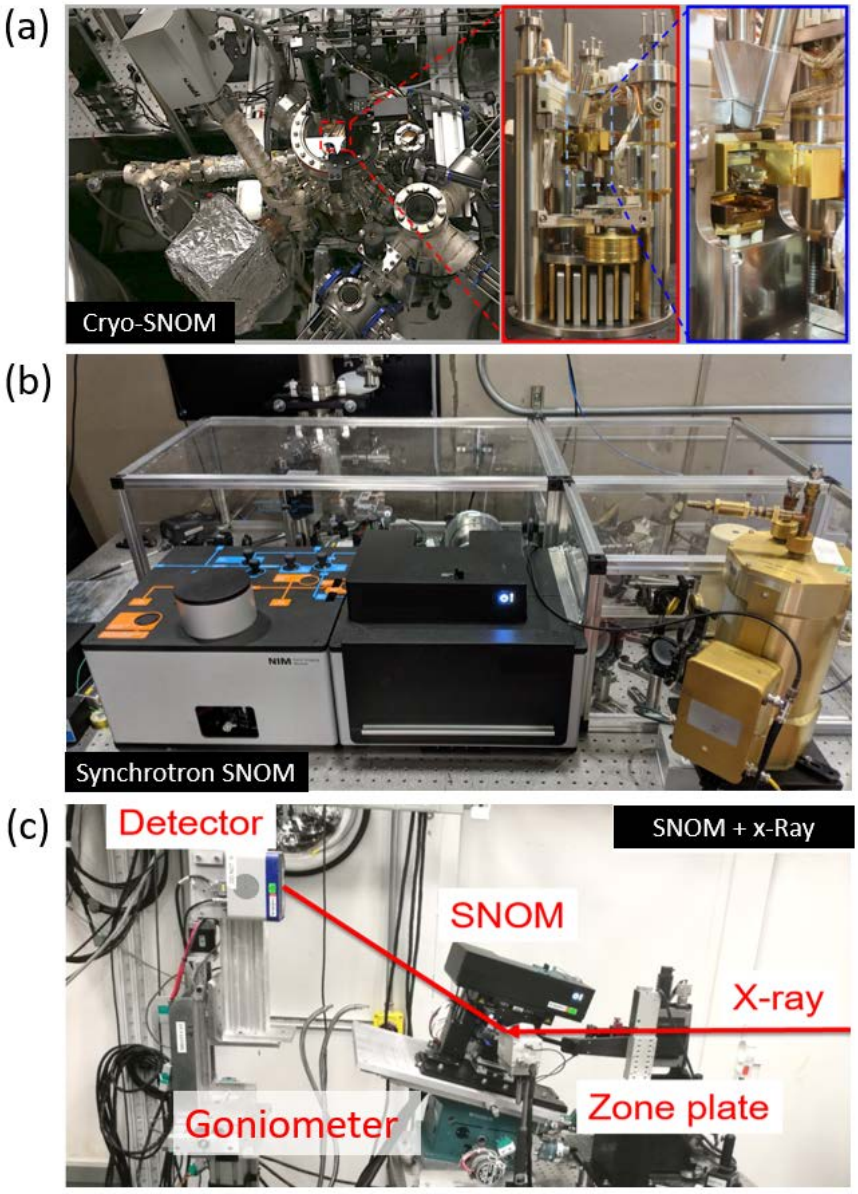

FIG 14 (a) cryo-SNOM set up currently in Professor Dimitri Basov's lab in Columbia University. (b) Synchrotron-based broadband s-SNOM in ALS, Berkeley. (c) A s-SNOM system integrated to a time-resolved x-ray diffraction microscopy beamline by Dr. Haidan Wen in Argonne National Laboratory.

IV. SIGNAL DETECTION SCHEMES

As briefly discussed in the introduction, in s-SNOM experiments the far-field-detected signal contains genuine near-field information as well as a strong and undesired background signal which comes from the far-field scattering of the tip and sample. This background signal causes unwanted artefacts and poses complications when extracting

optical properties of the samples. Therefore, a detection scheme that allows background filtration is necessary in s-SNOM experiments.

To suppress the background signal, the near-field signal is typically modulated by the AFM probe. In tapping mode, the AFM tip is oscillating vertically at its mechanical resonance frequency (Ω), typically at 20-300 kHz depending on the specific cantilever and driving voltage. The near-field signal varies rapidly with the tip-sample distance in a nonlinear fashion while the background signal varies strongly linear. Consequently, the demodulated scattering signal at the higher harmonics of the tip tapping frequency (2Ω, 3Ω...) predominantly contains near-field signal while the background is largely suppressed.

To optimally preserve the near-field signal and reduce the background signal, multiple detection schemes have been developed. In this article, we will focus our attention on intensity detection techniques. Electric field detection techniques like electro-optic sampling are viable methods, especially for THz and ultrafast s-SNOM, but are less common. Therefore, we will not discuss them explicitly. Among various intensity detection techniques, the most implemented are self-homodyne, homodyne, heterodyne, and pseudo-heterodyne. Here we introduce each method in detail with a simplified mathematical treatment and then present their advantages and disadvantages. Detailed mathematical derivations can be found in the respective references. Readers are also encouraged to read the in-depth review article by Dai *et al* [235].

Other less common, yet still successful, detection schemes such as phase-shifting interferometry [236] and the synthetic optical holography technique [237,238] have also been demonstrated successfully. Due to length constraint, we are not able to discuss them in detail.

A. Self-homodyne (SHD)

In the early stages of s-SNOM, the most common and straightforward detection scheme was self-homodyne detection as indicated in **FIG. 15** (a). The detector only records signal intensity, which is the amplitude squared of the incident electric field:

$$I = \left(\widetilde{E_n} + \widetilde{E_b}\right)\left(\widetilde{E_n^*} + \widetilde{E_b^*}\right),$$

where $\widetilde{E_n}$ is the complex near-field scattered electric field and $\widetilde{E_b}$ is the complex undesired background. * denotes the complex conjugate. Multiplying out the terms, it's easy to find that

$$I = \left|\widetilde{E_n}\right|^2 + 2\left|\widetilde{E_n}\right|\left|\widetilde{E_b}\right|\cos(\varphi_n - \varphi_b) + \left|\widetilde{E_b}\right|^2.$$

The lock-in amplifier demodulates the signal at higher harmonics of the tip tapping frequency. Since $\widetilde{E_b}$ varies little with tip-sample distance, $\left|\widetilde{E_b}\right|^2$ gets mostly filtered out after demodulation. Thus, the modulated signal becomes:

$$I = \left|\widetilde{E_n}\right|^2 + 2\left|\widetilde{E_n}\right|\left|\widetilde{E_b}\right|\cos(\varphi_n - \varphi_b).$$

That is, the detected signal contains a subtle combination of the near-field and background. Fortunately, in most cases, the second term is much larger than the first term because the background scattering is usually orders of magnitude larger than the near-field scattering. Thus, the detected signal can be structured into the near-field signal enhanced by the background signal. One major drawback of self-homodyne detection scheme is that only intensity information is accessible and phase information is totally lost because φ_b is not a controllable parameter, unlike more sophisticated detection schemes introduced in the following sessions. Furthermore, spatially varying $\widetilde{E_b}$ and φ_b could lead to a degree of randomness (artefact) in the obtained near-field images, making quantitative data interpretation difficult.

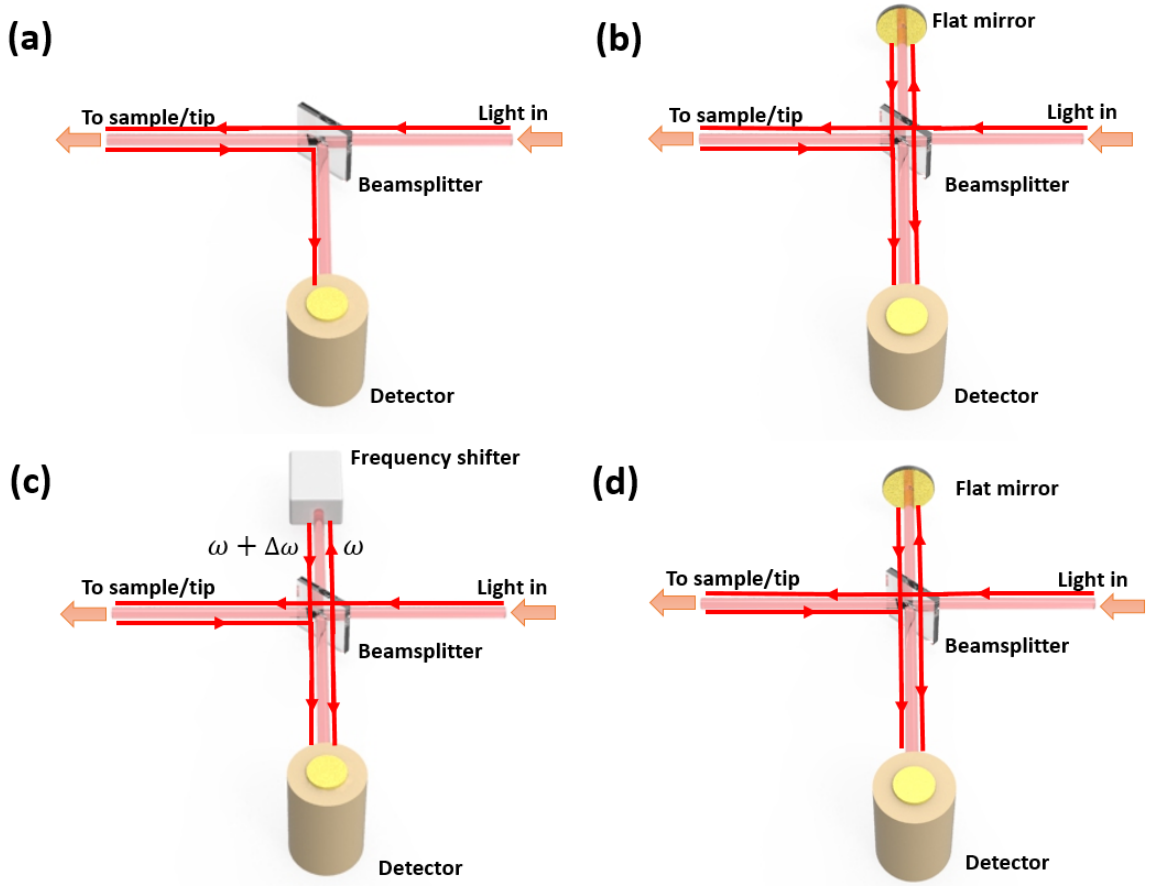

FIG 15. S-SNOM detection schemes. (a) Self-homodyne detection. (b) Homodyne detection. (c) Heterodyne detection. (d) Psedo-heterodyne detection.

B. Homodyne (HD)

Nowadays, self-homodyne detection is rarely used. Instead, a more advanced detection scheme, homodyne detection, is often utilized in a s-SNOM setup. Essentially, homodyne is self-homodyne with an added reference arm such that an asymmetric Michaelson interferometer is formed (**FIG. 15** (b)). With this coherent detection setup, both amplitude and phase information can be accessed. Looking at the detected signal intensity again, this time we have

$$I = \left(\widetilde{E_n} + \widetilde{E_b} + \widetilde{E_r}\right)\left(\widetilde{E_n^*} + \widetilde{E_b^*} + \widetilde{E_r^*}\right),$$

where $\widetilde{E_r}$ is the reference electric field. Multiplying out the terms, we arrive at

$$I = \left|\widetilde{E_n}\right|^2 + \left|\widetilde{E_b}\right|^2 + \left|\widetilde{E_r}\right|^2 + 2\left|\widetilde{E_n}\right|\left|\widetilde{E_b}\right|\cos(\varphi_n - \varphi_b) + 2\left|\widetilde{E_n}\right|\left|\widetilde{E_r}\right|\cos(\varphi_n - \varphi_r) + 2\left|\widetilde{E_b}\right|\left|\widetilde{E_r}\right|\cos(\varphi_b - \varphi_r).$$

After demodulation by the lock-in amplifier, the $\left|\widetilde{E_b}\right|^2$, $\left|\widetilde{E_r}\right|^2$, and $2\left|\widetilde{E_b}\right|\left|\widetilde{E_r}\right|\cos(\varphi_b - \varphi_r)$ terms become mostly filtered out since both $\widetilde{E_b}$ and $\widetilde{E_r}$ are not modulated by the tip tapping. Therefore, the detected signal becomes:

$$I = \left|\widetilde{E_n}\right|^2 + 2\left|\widetilde{E_n}\right|\left|\widetilde{E_b}\right|\cos(\varphi_n - \varphi_b) + 2\left|\widetilde{E_n}\right|\left|\widetilde{E_r}\right|\cos(\varphi_n - \varphi_r).$$

By deliberately raising the reference beam intensity much higher than the probing beam, the first two terms are small compared to the third. In effect, what we detect is the near-field term scaled by the reference signal. Since the reference beam's optical path can be easily adjusted, φ_r is in control. Therefore, coherent detection with both amplitude and phase is achieved.

Notice that with homodyne detection the second term containing the background cannot be totally neglected. Especially for reflective samples where $\widetilde{E_b}$ is large, background artefact will be present despite the demodulation procedure. A common way to minimize this is to place a reference (thick metal padding for example) right next to the sample. Dividing the signal detected on the sample by the signal detected on the reference can effectively get rid of the spatial variation caused by $\widetilde{E_b}$. Also, to obtain the complete information of both the amplitude and the phase information of the near-field signal, two consecutive scans with the reference mirror at different optical path lengths must be performed. The difference should be $\lambda/8$, or equivalently a quarter wavelength optical path difference or a 90 degree phase delay. For a highly reflective reference that only yields the real part of the near-field signal (as we will detail later), the real part of the signal can be found when the reference optical path matches the sampling optical path. The imaginary part is found when the difference between the two optical paths is half of the wavelength. This double-pass technique is relatively time-consuming and requires a

higher signal stability. However, the homodyne scheme is easy to implement compared to the more sophisticated techniques introduced in the following sections. Therefore, it is still one of the most commonly practiced detection methods [239].

C. Heterodyne (HTD)

In principle, the heterodyne detection [240–242] scheme can suppress the background signal completely. The major difference between heterodyne and homodyne is that the reference beam is frequency-shifted from the sampling beam in heterodyne detection while it stays the same in homodyne detection setup (**FIG. 15** (c)). In HTD after the beam leaves the beamsplitter the reference beam's frequency is shifted by a small amount, $\Delta\omega$. This frequency shift is commonly performed by an acousto-optic modulator (AOM). Mathematically speaking, the detected signal is still given by

$$I = \left(\widetilde{E_n} + \widetilde{E_b} + \widetilde{E_r}\right)\left(\widetilde{E_n^*} + \widetilde{E_b^*} + \widetilde{E_r^*}\right).$$

In the heterodyne case $\widetilde{E_r}$ denotes the frequency-shifted reference. Again, multiplying out the terms we arrive at

$$I = \left|\widetilde{E_n}\right|^2 + \left|\widetilde{E_b}\right|^2 + \left|\widetilde{E_r}\right|^2 + 2\left|\widetilde{E_n}\right|\left|\widetilde{E_b}\right|\cos(\varphi_n - \varphi_b) + 2\left|\widetilde{E_n}\right|\left|\widetilde{E_r}\right|\cos(\Delta\omega t + \varphi_n - \varphi_r) + 2\left|\widetilde{E_b}\right|\left|\widetilde{E_r}\right|\cos(\Delta\omega t + \varphi_b - \varphi_r).$$

After demodulation by the lock-in, $\left|\widetilde{E_b}\right|^2$ and $\left|\widetilde{E_r}\right|^2$ are essentially filtered out due to their time-independence. Note that $2\left|\widetilde{E_b}\right|\left|\widetilde{E_r}\right|\cos(\Delta\omega t + \varphi_b - \varphi_r)$ beats at frequency $\Delta\omega$ which provides a convenient reference for optical alignment of the interferometer. The $2\left|\widetilde{E_n}\right|\left|\widetilde{E_b}\right|\cos(\varphi_n - \varphi_b)$ term is mainly modulated at the tip tapping frequency, Ω. To extract the signal of interest, namely the $2\left|\widetilde{E_n}\right|\left|\widetilde{E_r}\right|\cos(\Delta\omega t + \varphi_n - \varphi_r)$ term, we perform demodulation at $n\Omega \pm \Delta\omega$ instead of $n\Omega$ in the homodyne case. To illustrate the reason for demodulating at $n\Omega \pm \Delta\omega$, we write $2\left|\widetilde{E_n}\right|\left|\widetilde{E_r}\right|\cos(\Delta\omega t + \varphi_n - \varphi_r)$ as a Fourier series:

$$\sum_k A_k \left|\widetilde{E_n}\right|\cos(k\Omega t)\left|\widetilde{E_r}\right|\cos(\Delta\omega t + \varphi_n - \varphi_r).$$

Therefore, when demodulated at $n\Omega \pm \Delta\omega$, the amplitude information mostly contains the near-field amplitude enhanced by the reference amplitude. The detected phase information is purely near-field since the reference phase and the frequency shift are artificially controllable quantities. No uncontrollable background is present.

D. Pseudo-heterodyne (PHD)

As discussed above, in the HTD scheme the reference beam is usually frequency-shifted by an AOM. This method is not universally applicable because commercially available AOMs only operate in a limited spectral range. To overcome this difficulty, the pseudo-heterodyne method was proposed and has been widely implemented [243–245]. The pseudo-heterodyne detection setup (**FIG. 15** (d)) is similar to the HD setup. The only difference is that in the PHD scheme the reference mirror is vibrating harmonically with a small spatial amplitude, a at a frequency ω_m much smaller than the AFM probe vibration frequency, Ω. This vibration changes the optical path of the reference arm causing a phase-modulation of the reference beam electric field. This electric field can be written in Fourier series as

$$\widetilde{E_r} = \sum_k A_k e^{ik\omega_m t},$$

where the Fourier coefficients are given by

$$A_k = AJ_k(a)e^{i(\frac{k\pi}{2}+\Delta\varphi)},$$

where J_n is the k-th Bessel function of the first kind and $\Delta\varphi$ is the phase difference between the reference beam and sampling beam. Due to this phase-modulation of the reference arm, the n-th harmonics of the detected signal split into sidebands at frequencies $n\Omega \pm m\omega_m$. Notice that among the sidebands the signal is successively proportional to the real and imaginary part of the complex signal. By setting the modulation amplitude a to a specified value, the proportionality of the real and imaginary parts can be equalized. Thus, the pseudo-heterodyne detection scheme allows simultaneous measurement of the signal amplitude and phase (or more directly, real and imaginary parts) in one raster scan yielding superior time efficiency.

The superior time-efficiency and background-free nature of PHD allow this technique to be commonly practiced and is performed by many researchers pursuing PhD degrees in near-field optics today.

V. ANALYTICAL MODELS AND NUMERICAL METHODS

The complex nature of propagating and non-propagating waves in near field detection poses great difficulties to data interpretation. Understanding the scattering pattern of the important “mediator” and “scatter” - the tip - which initiates both the near-field and free space far-field waves is the first step to decipher the sample properties encoded in the near-field signals [246]. In addition, due to the strong coupling of the tip and the sample each loses their own identity and they become a single entity. Thus, we must treat a scattering problem of the tip-sample ensemble. The intrinsic length scale for this tip-

sample ensemble is on the deep subwavelength scale which sometimes poses challenges for calculation using classical electrodynamic theory. In addition, the tip geometry approximates a cone which creates a non-integrable singularity point and length scale mismatch near the tip apex. As a result, analytical modeling or numerical simulation is hard to perform due to calculation divergences and large mesh cell settings, respectively. Nevertheless, with decades of development the complexity and predictability of the theoretical and simulation methods have advanced significantly. Various geometries including spheres, elongated spheroids, hyperboloids, and cones have been employed to approximate the role of the tip (**FIG**. **16** (a)). In the following section, we will introduce in detail various representative models. We will also compare the predictability of these models with a representative sample: SiO_2 at its IR active phonon frequency close to ~1100 cm^{-1}.

We also want to mention that the localized field at the vicinity of tip-sample gap contains a broad momentum distribution. Qualitatively, the dominant momentum is on the order of 1/(tip radius). In some cases, especially in good metals, 2D materials, and thin films, nonlocality has a significant effect. That is, the sample properties like the permittivity and conductivity not only depend on frequency but also pick up a momentum dependence. The nonlocal effect will be discussed at the end of this section.

A. Momentum-dependent reflection coefficient

A straightforward but crude approximation for understanding s-SNOM reflectivity is the so-called " r_p approximation" [6], with the p denoting the p-polarized electric field of the incident wave. In this approximation we completely ignore the geometry of the tip and only account for its presence by considering the momentum-dependent sample response. This is given by the momentum-dependent p-polarized reflectivity [247]

$$r_p(\omega, q) = \frac{\varepsilon_1 k_0 - \varepsilon_0 k_1}{\varepsilon_1 k_0 + \varepsilon_0 k_1}, \qquad (1)$$

where ε_0 denotes vaccum permittivity and ε_1 denotes sample permittivity. k_0 and k_1 denote z-components of the momenta in vaccum and sample and are given by

$$k_{0,1} = \sqrt{\varepsilon_{1,2}\frac{\omega^2}{c^2} - q^2}, \qquad (2)$$

where ω is the light's frequency and q is the in-plane component of the momentum. Since the confined electric field is evanescent, the imaginary part of $k_{0,1}$ must be a positive nonzero number. Due to the tip scattering, the near-field electromagnetic wave has a wide range of in-plane momentum distribution with most of its weight much larger than the free space momentum. The q distribution follows a weight function which peaks

at roughly $\sim\frac{1}{a}$ where a is the tip apex curvature radius with a typical value of 10 to 100 nm. Since generally $q \gg \frac{\omega}{c}$, r_p can be further approximated by the q-independent function which is found by taking the limit as $q \to \infty$:

$$r_p(\omega) = \frac{\varepsilon_1 - \varepsilon_0}{\varepsilon_1 + \varepsilon_0} = \frac{\varepsilon_1 - 1}{\varepsilon_1 + 1}. \qquad (3)$$

We need to stress that the r_p approximation only provides the simplest understanding of the physical process in a near-field experiment so it is not expected to have any quantitative predictability. However, its importance should not be overlooked as it functions as a stepping stone for the future developments of more complicated models. Several studies, mostly involving two-dimensional materials, have been successfully understood by this simple approach [174,248].

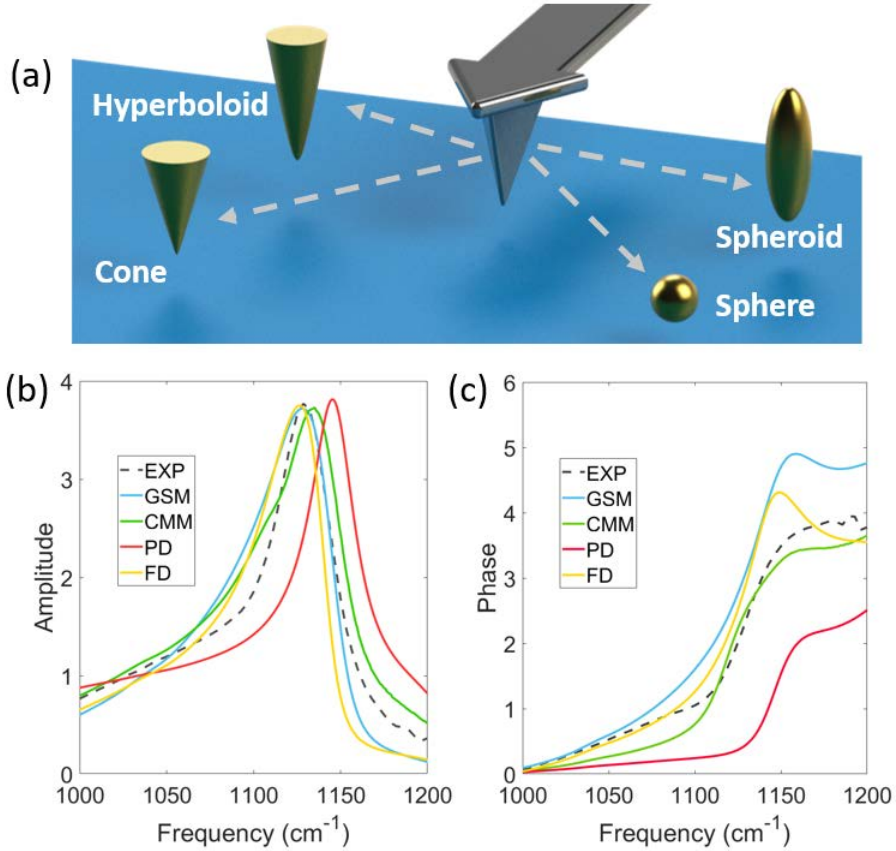

FIG 16. (a) Schematic representation of various geometries including a sphere, elongated spheroid, hyperboloid, and cone for tip approximation in theoretical models. Third harmonic near-field amplitude (b) and phase (c) spectra calculated by various models compared to experimentally measured data as a benchmark for model predictability. Experimental data is adapted from ref [249]**. GSM: generalized spectral method; CMM: conformal mapping method; PD: point-dipole mode; FD: finite-dipole mode; EXP: experimental data.**

B. Point-Dipole Model

Heavy theoretical investigations of the behavior of a polarized particle above an infinite plane have been carried out since over half contrary ago [247,250–255]. In the late 1990s, this model was applied to s-SNOM for data interpretation [256]. To account for the presence of the tip, the most straightforward approach is to approximate the tip as a polarized sphere and then as a point dipole with the same polarizability [44,257,258]. This model, both in its original version and modified versions, has successfully explained much of the experimental data at least on a qualitative level [174,182,259–261]. With this approximation the problem at hand essentially becomes a scattering problem of light by a small particle (AFM tip) above an infinite half space (sample). Rigorous mathematical treatment of this problem can be found in **ref** [247,262,263]. For our purposes, we only catch the essence of this model without going into the details. Also, we will only present the simplest version of the point-dipole model where (1) the sample is considered as an isotropic infinite half space, (2) we only consider the vertical component of the electric field, and (3) we make use of the quasi-electrostatic approximation where retardation is ignored. Note that more complex versions of the point-dipole model have been developed over the years as well such as the point-dipole model for the anisotropic sample [264] and the point-dipole model for the multilayer sample [161]. Retardation and multiple scattering effects have also been considered [265]. Furthermore, beyond the dipole approximation, the multipole moment of the probe has been taken into consideration [265,266]. In 2011, a modified dipole model for THz s-SNOM analysis was proposed by Moon *et al* [260]. All these modifications have made the point-dipole model more generic and show improved consistency with experimental results.

In its simplest form the AFM tip is approximated as a polarized sphere with dielectric constant ε_t and radius a located at position $(0,0,z+a)$. In most cases, ε_t is assumed to be constant in the frequency of interest. The polarizability of the sphere is given by

$$\alpha = 4\pi a^3 \frac{\varepsilon_t - \varepsilon_i}{\varepsilon_t + 2\varepsilon_i}, \quad (4)$$

where ε_i is the dielectric constant of the surrounding medium. In our case, the tip is typically in an ambient condition so we can take $\varepsilon_i = 1$ and

$$\alpha = 4\pi a^3 \frac{\varepsilon_t - 1}{\varepsilon_t + 2}. \quad (5)$$

To further simplify the mathematics, we can replace the sphere with a point dipole of equal strength. Now we consider the sample: the infinite half space, $z < 0$. The classical method of image can be applied here. Equivalently, consider an image dipole with polarizability $\alpha\beta$ located at $(0,0,-(a+z))$, where $\beta = \frac{\varepsilon_s - 1}{\varepsilon_s + 1}$ is the dielectric surface response function (same as the r_p model discussed in the previous sub-section) and ε_s is the sample's dielectric constant.

It is the interaction between the tip dipole and the sample dipole that catches the essence of the near-field response that we observe in s-SNOM experiments. Using Maxwell's equations under the electrostatic limit, we conclude that the effective polarizability of the tip-sample system is given by

$$\alpha_{eff} = \frac{\alpha(1+\beta)}{1-\alpha\beta/(16\pi(a+z)^3)}. \quad (6)$$

The scattered field is known to be proportional to the polarizability. Finally, to compare this result with the experimental data it is crucial to demodulate α_{eff} at higher harmonics of the probe oscillation frequency, i.e.

$$\mathrm{S_n} \sim \int_0^T \alpha_{eff}\,(z(t),\omega) e^{in\Omega t} dt, \quad (7)$$

where $\mathrm{S_n}$ represents the n-th harmonics near-field signal, Ω is the tip oscillation frequency and $\mathrm{T} = \frac{2\pi}{\Omega}$ is the tip oscillation period.

C. Finite-dipole Model

Despite its simplicity, the point-dipole model shows relatively poor quantitative predictability for slightly more complex systems such as a strongly resonant sample. This is mostly due to its inaccurate approximation of the tip geometry. More specifically, the elongated shape of the realistic tips is totally ignored which can underestimate the antenna effect. To further advance the model, an elongated spheroid-shaped tip was considered in the late 2000s [267]. Here we briefly discuss some important results of the finite-dipole model. A more detailed derivation can be found in **ref** [267].

Based on a previous study of a conducting prolate spheroid under illumination [268], it is known that to obtain a good approximation of the physical situation, we only need to consider localized charges near the end of the spheroid. The fraction of localized charge to induced total charge g, depends on the tip-sample distance but becomes relatively constant close to 0.7. Again, using the image method we conclude that the effective polarizability of the spheroid is given by

$$\alpha_{eff} = R^2 L \frac{\frac{2L}{R} + \ln\frac{R}{4eL}}{\ln\frac{4L}{e^2}} \left(2 + \frac{\beta\left(g - \frac{R+H}{L}\right)\ln\frac{4L}{4H+3R}}{\ln\frac{4L}{R} - \beta\left(g - \frac{3R+4H}{4L}\right)\ln\frac{2L}{2H+R}}\right), \quad (8)$$

where R is the tip apex radius, L is the tip length, H is the tip-sample distance, g is roughly 0.7 as mentioned above, and $\beta = \frac{\varepsilon_s - 1}{\varepsilon_s + 1}$ as in the point dipole model.

Due to the spheroid's elongated length, the tip's role as a light-confining antenna is reproduced very well and maintains better quantitative consistency with the experimental data [269].

D. Models beyond a closed-form solution

In both the point-dipole and the finite-dipole models an analytical expression of α_{eff} can be found which makes these models easy to implement. More mathematically rigorous treatments of the tip with spheroid or hyperboloid related shapes have been further considered to improve the accuracy of the predictions. Mathematical details are omitted in this article due to their complexity but can be found in [249,270]. With those treatments a superior predictability is achieved. It is instructive to note that as pointed out by Yang *et al*. in **ref** [270], the point-dipole model and the finite-dipole model attempt to approximate a continuous charge distribution with a point source. As a consequence, only the lowest order localized surface mode is preserved and higher order modes are ignored. This can lead to quantitative inaccuracies especially when the sample material has strong resonances.

A more intriguing and realistic tip geometry, namely a cone, has never been analytically considered until recently because of the non-integrable singularity at the top of the tip. This difficulty has been circumvented by the conformal mapping method. With conformal mapping a cone-shaped tip geometry can finally be considered. This pioneering method shows great quantitative agreement with experiments. Additionally, not only does this method show quantitatively consistent predictions, it also yields high time-efficiency. The calculation can be done in seconds which is superior even when compared to simpler models. Mathematical details are omitted here but can be found in **ref** [271].

As a benchmark for the performance of the models introduced above, we carry out calculations of the near-field spectra in 1000-1200 cm^{-1} for the representative material SiO_2. SiO_2 is a great candidate because it is well known that SiO_2 exhibits a phonon-polariton mode at ~1130 cm^{-1} which shows a distinct response in the spectrum. Calculations based on the point-dipole model (PD), finite-dipole model (FD), generalized spectral method (GSM), and conformal mapping method (CMM), as well as an experimental (EXP) measurement are shown in **FIG.** 16 (b) and (c). The progressing predictability of these models, especially in the phase spectra, is evident.

E. Numerical Methods

Aside from analytical treatment, full wave simulations using various algorithms including finite element method, finite-difference-time-domain method, and so on can also be employed to model the scattered signal. Various commercially available solvers like CST Microwave STUDIO, Lumerical FDTD, and CONSOL MULTIPHYSICS provide convenient modeling platforms and effective calculation algorithms. The geometry of the tip and sample can be represented with minimum approximation. Several studies have employed the signal demodulation procedure in simulations and obtained quantitatively consistent

results [272–274]. More straightforward methods without considering tip modulation have also been implemented by simply regarding the electric field intensity between the tip and the sample as proportional to the near-field signal. Due to its time-efficiency, using the electric field intensity near sample surface to approximate the near-field signal is also a common practice especially for studies of plasmonic nanostructures [129,131–133,151,261,275–277].

F. Nonlocality in s-SNOM

In previous discussions, we only explicitly considered the frequency dependence of the sample permittivity. It is important to note that in general there is a momentum dependence as well (nonlocality). Here we only briefly touch the surface of this nonlocal effect which deserves much more attention in the future.

There are three crucial relevant length scales in a s-SNOM measurement. These are the free space wavelength λ, the tip apex radius a, and the particle or quasiparticle mean free path of the sample material d. Correspondingly, there are three relevant momentum scales: free space light momentum $q_1 = \frac{\omega}{c} = \frac{2\pi}{\lambda}$, confined (near-field) wave momentum $q_2 \sim \frac{1}{a}$, and particle or quasiparticle momentum $q_3 = \frac{\omega}{v_F} \sim \frac{2\pi}{d}$, where v_F is the Fermi velocity of the material and d is the distance that a quasiparticle can travel within one period of the electromagnetic oscillation. Typically, the condition $q_1 \ll q_2 \ll q_3$ is met because $d \leq a \leq \lambda$. Under this condition, quasistatic treatment of the tip-sample interaction (no retardation) and local approximation of the sample's optical constant ($\varepsilon(\omega, q) \rightarrow \varepsilon(\omega)$) can be justified. However, in some cases where ω is small, e.g. with THz or microwave illuminations, q_2 can become comparable to or even larger than q_3. Thus, the local approximation breaks down. To account for the nonlocality, the momentum dependence of the optical constant has to be carefully addressed. So far, this intrinsic nonlocality has only been observed and theoretically understood within s-SNOM experiments in low-dimensional materials like graphene [5,218] and plasmonic nanostructures made of noble metals [130].

VI. Others

Since s-SNOM is an ever-growing field, it's impractical to cover all the aspects in this short review. There are many near-field related measurements performed in a way that are different from the main concepts introduced in this article. Here, we mention a few novel ideas related to this research frontier.

(1) By applying an intense pulsed laser source, AFM-IR does not detect the scattered light. Instead, it directly probes the oscillation of the AFM tip in contact mode to yield the IR absorption spectrum via nano-thermal expansion of the sample surface [278–291].
(2) Komiyama *et al.* recently proposed an interesting method to investigate sample's thermal radiation with s-SNOM [292]. In their work, they used a passive imaging technique where the thermal evanescent waves from the sample surface directly provided near-field interaction with the tip and eventually scattered into the far-field.
(3) Operating s-SNOM in peak-force mode is another innovative technique [293–295]. With this method, the mechanical properties of the sample can be simultaneously accessed in parallel to the optical information.
(4) Furthermore, current resolution of s-SNOM is predominantly limited by the curvature radius of the tip apex. Without making it sharper, a new method to improve resolution has been proposed very recently. Greener *et al.* demonstrated that by using two excitation sources with different frequencies instead of one, they can greatly enhance the spatial resolution of imaging [296]. Future research is still needed to advance this idea. In addition, a number of studies on how to improve the probing tip have also been performed [297–302].

VII. SUMMARY AND OUTLOOK

The task of deterministic characterization of optical properties over a broad spectral range down to nanometer resolution is a grand challenge. The fact that the tip is inseparable from model analysis provides us with both obstacles and opportunities. This review merely scratched the surface of this subject, by introducing the basics of detection schemes and data interpretation. The continual desire for finer spatial resolution might eventually force one to redefine the use of macroscopic optical parameters which are based on the validity of the concept of quasiparticles, e.g. the semiclassical treatment of dielectric constant. For instance, when both the tip and sample become quantum objects where discrete optical states can exist, a true quantum entangled between the tip and sample may be established. The quantum back action, information storage, and causality can then become important subjects to study [303–305].

Of course, before the fruition of near-field quantum optics, many taunting tasks remains to be accomplished. One of the most attainable goals in the near future is to measure the momentum dependent nonlocality at cryogenic temperatures with low energy photo-excitation. Investigations with a more surgical control of the tip modality, further improvement of the theoretical modeling of sample inhomogeneity and anisotropy, and

a full consideration of the local magnetic, thermal, and aerodynamics environment will all be important future prospects to tackle.

By coupling s-SNOM to ultrafast optics, nano-XRD, Raman, and perhaps STM, the next generation multimodal imaging tools for material characterization are quickly emerging. This not only applicable to the field of condensed matter physics, but also to broader communities including chemistry, biology, and various fields of engineering. With the immense amount of growing experimental data, it will be beneficial to create efficient ways for the community to organize, compare, and collaborate. Interactive database, systematic imaging analysis, and "deep learning" procedure can greatly enhance the field as whole. From Synge's original proposal in 1928 to s-SNOM's current experimental success, much has been learned during the 90 years. A summary showcasing some iconic phenomena and its characteristic frequency and time scale is listed in **FIG. 17**. As we can see, a wide frequency range, from visible to THz, has been covered. Yet, s-SNOM is still in its adolescence and its progression into becoming a mature field will surely make it an indispensable tool to explore the nanoworld.

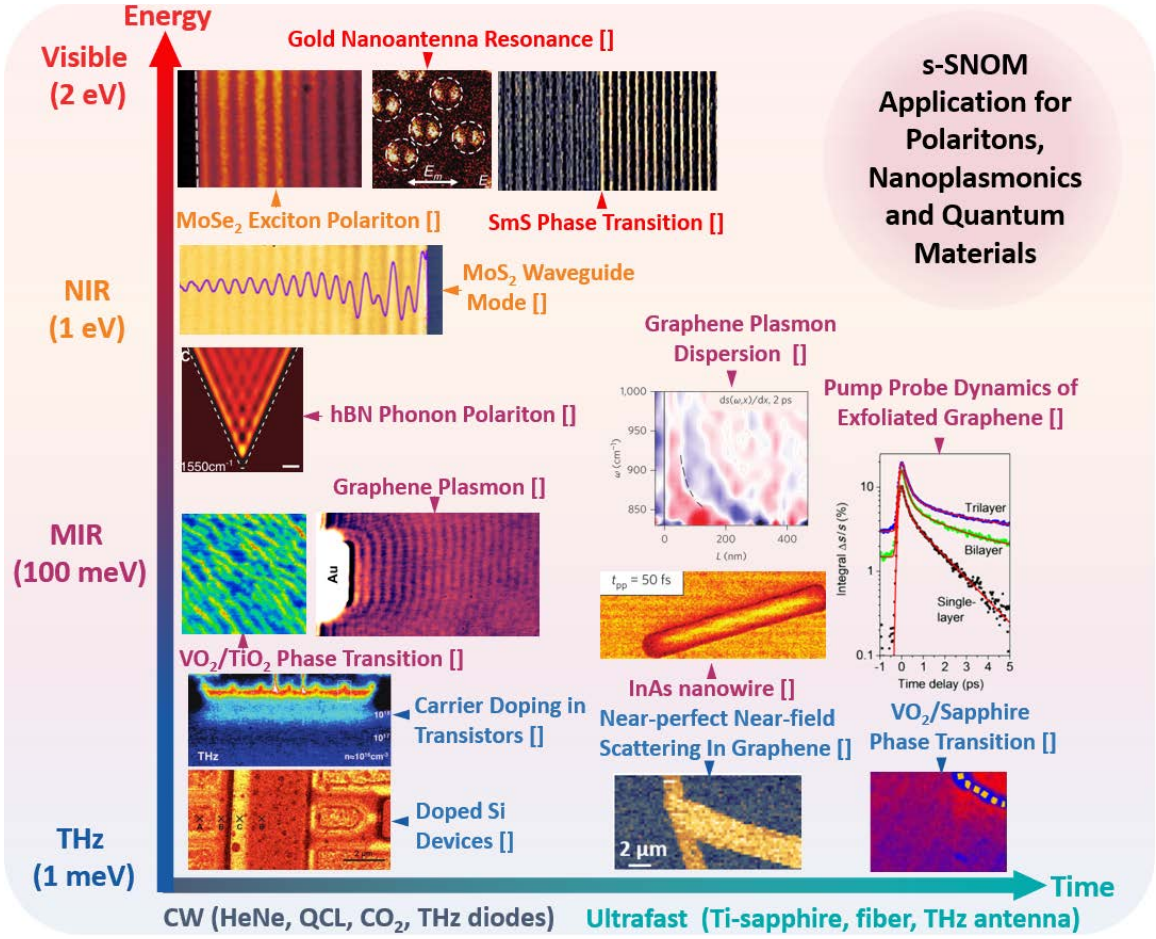

FIG 17. Summary of the applications of s-SNOM, showing some iconic phenomena in characteristic frequency and time scale. (reference number will be added later)

Acknowledgment

We thank Alexander S. McLeod, Wenjie Wang (Ithatron optics), Andrea (Andy) Huber (Neaspec inc.), G. Lawrence (Larry) Carr, Hans A. Bechtel, Michael Martin, Haidan Wen, S. T (Tat) Chui, and Gregory (Greg) O. Andreev for helpful discussions.

References

[1] E. Abbe, Arch. Für Mikroskopische Anat. **9**, 413 (1873).

[2] A. S. McLeod, E. van Heumen, J. G. Ramirez, S. Wang, T. Saerbeck, S. Guenon, M. Goldflam, L. Anderegg, P. Kelly, A. Mueller, M. K. Liu, I. K. Schuller, and D. N. Basov, Nat. Phys. **13**, 80 (2016).

[3] M. M. Qazilbash, M. Brehm, B.-G. Chae, P.-C. Ho, G. O. Andreev, B.-J. Kim, S. J. Yun, A. V Balatsky, M. B. Maple, F. Keilmann, H.-T. Kim, and D. N. Basov, Science (80-.). **318**, 1750 (2007).

[4] J. Chen, M. Badioli, P. Alonso-González, S. Thongrattanasiri, F. Huth, J. Osmond, M. Spasenović, A. Centeno, A. Pesquera, P. Godignon, A. Zurutuza Elorza, N. Camara, F. J. G. de Abajo, R. Hillenbrand, and F. H. L. Koppens, Nature **487**, 77 (2012).

[5] Z. Fei, A. S. Rodin, G. O. Andreev, W. Bao, A. S. McLeod, M. Wagner, L. M. Zhang, Z. Zhao, M. Thiemens, G. Dominguez, M. M. Fogler, A. H. C. Neto, C. N. Lau, F. Keilmann, and D. N. Basov, Nature **487**, 82 (2012).

[6] S. Dai, Z. Fei, Q. Ma, A. S. Rodin, M. Wagner, A. S. McLeod, M. K. Liu, W. Gannett, W. Regan, K. Watanabe, T. Taniguchi, M. Thiemens, G. Dominguez, A. H. C. Neto, A. Zettl, F. Keilmann, P. Jarillo-Herrero, M. M. Fogler, and D. N. Basov, Science (80-.). **343**, 1125 (2014).

[7] B. Pollard, E. A. Muller, K. Hinrichs, and M. B. Raschke, Nat. Commun. **5**, 3587 (2014).

[8] H. A. Bechtel, E. A. Muller, R. L. Olmon, M. C. Martin, and M. B. Raschke, Proc. Natl. Acad. Sci. **111**, 7191 (2014).

[9] A. Bouhelier, Microsc. Res. Tech. **69**, 563 (2006).

[10] E. A. Muller, B. Pollard, and M. B. Raschke, J. Phys. Chem. Lett. **6**, 1275 (2015).

[11] B. Kästner, C. M. Johnson, P. Hermann, M. Kruskopf, K. Pierz, A. Hoehl, A. Hornemann, G. Ulrich, J. Fehmel, P. Patoka, E. Rühl, and G. Ulm, ACS Omega **3**, 4141 (2018).

[12] M. Filimon, I. Kopf, F. Ballout, D. A. Schmidt, E. Bründermann, J. Rühe, S. Santer, and M. Havenith, Soft Matter **6**, 3764 (2010).

[13] T. Craig, A. D. Smith, G. M. Holder, J. Ingham, C. I. Smith, A. Varro, D. M. Pritchard, S. D. Barrett, D. S. Martin, P. Harrison, A. Wolski, A. Cricenti, M. Luce, M. Surman, S. Chattopadhyay, P. Weightman, and M. R. F. Siggel-King, Phys. Status Solidi **1700518**, 1700518 (2018).

[14] J. Jiang, S. Zhang, Z. Qian, N. Qin, W. Song, L. Sun, Z. Zhou, Z. Shi, L. Chen, X. Li, Y. Mao, D. L. Kaplan, S. N. Gilbert Corder, X. Chen, M. Liu, F. G. Omenetto, X. Xia, and T. H. Tao, Adv. Mater. **1705919**, 1705919 (2018).

[15] I. Kopf, C. Grunwald, E. Bründermann, L. Casalis, G. Scoles, and M. Havenith, J. Phys. Chem. C **114**, 1306 (2010).

[16] D. Perez-Guaita, K. Kochan, M. Batty, C. Doerig, J. Garcia-Bustos, S. Espinoza, D. McNaughton, P. Heraud, and B. R. Wood, Anal. Chem. **90**, 3140 (2018).

[17] N. Qin, S. Zhang, J. Jiang, S. G. Corder, Z. Qian, Z. Zhou, W. Lee, K. Liu, X. Wang, X. Li, Z. Shi, Y. Mao, H. A. Bechtel, M. C. Martin, X. Xia, B. Marelli, D. L. Kaplan, F. G. Omenetto, M. Liu, and T. H. Tao, Nat. Commun. **7**, 13079 (2016).

[18] S. Berweger, D. M. Nguyen, E. A. Muller, H. A. Bechtel, T. T. Perkins, and M. B. Raschke, J. Am. Chem. Soc. **135**, 18292 (2013).

[19] M. Paulite, Z. Fakhraai, I. T. S. Li, N. Gunari, A. E. Tanur, and G. C. Walker, J. Am. Chem. Soc. **133**, 7376 (2011).

[20] M. Brehm, T. Taubner, R. Hillenbrand, and F. Keilmann, Nano Lett. **6**, 1307 (2006).

[21] S. Amarie, P. Zaslansky, Y. Kajihara, E. Griesshaber, W. W. Schmahl, and F. Keilmann, Beilstein J. Nanotechnol. **3**, 312 (2012).

[22] I. Amenabar, S. Poly, W. Nuansing, E. H. Hubrich, A. A. Govyadinov, F. Huth, R. Krutokhvostov, L. Zhang, M. Knez, J. Heberle, A. M. Bittner, and R. Hillenbrand, Nat. Commun. **4**, 1 (2013).

[23] O. Khatib, J. D. Wood, A. S. McLeod, M. D. Goldflam, M. Wagner, G. L. Damhorst, J. C. Koepke, G. P. Doidge, A. Rangarajan, R. Bashir, E. Pop, J. W. Lyding, M. H. Thiemens, F. Keilmann, and D. N. Basov, ACS Nano **9**, 7968 (2015).

[24] B. J. Bohn, M. Schnell, M. A. Kats, F. Aieta, R. Hillenbrand, and F. Capasso, Nano Lett. **15**, 3851 (2015).

[25] M. Schnell, P. Sarriugarte, T. Neuman, A. B. Khanikaev, G. Shvets, J. Aizpurua, and R. Hillenbrand, Nano Lett. **16**, 663 (2016).

[26] A. J. Huber, F. Keilmann, J. Wittborn, J. Aizpurua, and R. Hillenbrand, Nano Lett. **8**, 3766 (2008).

[27] a J. Huber, J. Wittborn, and R. Hillenbrand, Nanotechnology **21**, 235702 (2010).

[28] A. J. Huber, D. Kazantsev, F. Keilmann, J. Wittborn, and R. Hillenbrand, Adv. Mater. **19**, 2209 (2007).

[29] A. Gozar, N. E. Litombe, J. E. Hoffman, and I. Božović, Nano Lett. **17**, 1582 (2017).

[30] J. Rensberg, S. Zhang, Y. Zhou, A. S. McLeod, C. Schwarz, M. Goldflam, M. Liu, J. Kerbusch, R. Nawrodt, S. Ramanathan, D. N. Basov, F. Capasso, C. Ronning, and M. A. Kats, Nano Lett. **16**, 1050 (2016).

[31] G. Dominguez, A. S. Mcleod, Z. Gainsforth, P. Kelly, H. A. Bechtel, F. Keilmann, A. Westphal, M. Thiemens, and D. N. Basov, Nat. Commun. **5**, 5445 (2014).

[32] B. K. J. Rosenfeld, in *Clim. Chang. 2013 - Phys. Sci. Basis*, edited by Intergovernmental Panel on Climate Change (Cambridge University Press, Cambridge, 1935), pp. 1–30.

[33] C. R. Burch and J. P. P. Stock, J. Sci. Instrum. **19**, 71 (1941).

[34] W. Lang, ZEISS Inf. 114 (1968).

[35] M. J. Solomon and M. Kogan, Encycl. Condens. Matter Phys. **1**, 229 (2005).

[36] E. Wolf and M. Nieto-Vesperinas, J. Opt. Soc. Am. A **2**, 886 (1985).

[37] C. Girard, C. Joachim, and S. Gauthier, Reports Prog. Phys. **63**, 893 (2000).

[38] C. Girard and A. Dereux, Reports Prog. Phys. **59**, 657 (1996).

[39] C. Girard, Reports Prog. Phys. **68**, 1883 (2005).

[40] T. G. Rochow and E. G. Rochow, in *An Introd. to Microsc. by Means Light. Electrons, X-Rays, or Ultrasound* (Springer US, Boston, MA, 1978), pp. 273–298.

[41] G. Binnig, H. Rohrer, C. Gerber, and E. Weibel, Phys. Rev. Lett. **49**, 57 (1982).

[42] D. B. Williams and C. B. Carter, *Transmission Electron Microscopy: A Textbook for Materials Science* (2009).

[43] J. Crawford and J. Brown, Libr. Hist. **23**, 267 (2007).

[44] F. Keilmann and R. Hillenbrand, Philos. Trans. A. Math. Phys. Eng. Sci. **362**, 787 (2004).

[45] S. Patane, P. G. Gucciardi, M. Labardi, and M. Allegrini, Riv. Del Nuovo Cim. **27**, 1 (2004).

[46] B. T. Rosner and D. W. Van Der Weide, Rev. Sci. Instrum. **73**, 2505 (2002).

[47] D. Courjon and C. Bainier, Reports Prog. Phys. **57**, 989 (1994).

[48] E. Bründermann and M. Havenith, Annu. Reports Sect. “C” (Physical Chem. **104**, 235 (2008).

[49] A. Centrone, Annu. Rev. Anal. Chem. **8**, 101 (2015).

[50] W. Adams, M. Sadatgol, and D. Ö. Güney, AIP Adv. **6**, 100701 (2016).

[51] E. Synge, Phil. Mag **6**, 356 (1928).

[52] E. H. Synge, London, Edinburgh, Dublin Philos. Mag. J. Sci. **13**, 297 (1932).

[53] J. A. O'Keefe, J. Opt. Soc. Am. **46**, 359 (1956).

[54] J. Wessel, J. Opt. Soc. Am. B **2**, 1538 (1985).

[55] K. Karraï and R. D. Grober, Ultramicroscopy **61**, 197 (1995).

[56] D. W. Pohl, W. Denk, and M. Lanz, Appl. Phys. Lett. **44**, 651 (1984).

[57] U. Dürig, D. W. Pohl, and F. Rohner, J. Appl. Phys. **59**, 3318 (1986).

[58] E. Betzig, A. Lewis, A. Harootunian, M. Isaacson, and E. Kratschmer, Biophys. J. **49**, 269 (1986).

[59] E. Betzig and J. K. Trautman, Science (80-.). **257**, 189 (1992).

[60] E. Betzig, a Harootunian, a Lewis, and M. Isaacson, Appl. Opt. **25**, 1890 (1986).

[61] E. Ash and G. Nicholls, Nature **237**, 510 (1972).

[62] E. Betzig, Rev. Mod. Phys. **87**, 1153 (2015).

[63] B. Hecht, B. Sick, U. P. Wild, V. Deckert, R. Zenobi, O. J. F. Martin, and D. W. Pohl, J. Chem. Phys. **112**, 7761 (2000).

[64] R. Ivanov, S. Marcinkevičius, M. D. Mensi, O. Martinez, L. Y. Kuritzky, D. J. Myers, S. Nakamura, and J. S. Speck, Phys. Rev. Appl. **7**, 064033 (2017).

[65] Y. T. Chen, K. F. Karlsson, J. Birch, and P. O. Holtz, Sci. Rep. **6**, 21482 (2016).

[66] E. U. Haq, Z. Liu, Y. Zhang, S. A. A. Ahmad, L.-S. Wong, S. P. Armes, J. K. Hobbs, G. J. Leggett, J. Micklefield, C. J. Roberts, and J. M. R. Weaver, Nano Lett. **10**, 4375 (2010).

[67] Y. Nishiyama and H. Okamoto, J. Phys. Chem. C **120**, 28157 (2016).

[68] H. Mizobata, S. Hasegawa, and K. Imura, J. Phys. Chem. C **121**, 11733 (2017).

[69] Y. Kawakami, A. Kaneta, A. Hashiya, and M. Funato, Phys. Rev. Appl. **6**, 044018 (2016).

[70] J. Nozaki, M. Fukumura, T. Aoki, Y. Maniwa, Y. Yomogida, and K. Yanagi, Sci. Rep. **7**, 46004 (2017).

[71] R.-H. Jiang, C. Chen, D.-Z. Lin, H.-C. Chou, J.-Y. Chu, and T.-J. Yen, Nano Lett. **18**, 881 (2018).

[72] M. Kim, S. Choi, J.-H. Lee, C. Park, T.-H. Chung, J. H. Baek, and Y.-H. Cho, Sci. Rep. **7**, 42221 (2017).

[73] K. Imaeda, S. Hasegawa, and K. Imura, J. Phys. Chem. C **122**, 7399 (2018).

[74] Y. Lee, S. J. Yun, Y. Kim, M. S. Kim, G. H. Han, A. K. Sood, and J. Kim, Nanoscale **9**, 2272 (2017).

[75] Z. Cao, M. Ermes, S. Lehnen, R. Carius, and K. Bittkau, Phys. Chem. Chem. Phys. **20**, 1098 (2018).

[76] Y. Lee, S. Park, H. Kim, G. H. Han, Y. H. Lee, and J. Kim, Nanoscale **7**, 11909 (2015).

[77] S. Baral, A. Rafiei Miandashti, and H. H. Richardson, Nanoscale 941 (2018).

[78] S. Ezugwu, S. Kazemian, D.-Y. W. Choi, and G. Fanchini, Nanoscale **9**, 4097 (2017).

[79] A. C. Jones and M. B. Raschke, Nano Lett. **12**, 1475 (2012).

[80] S. Ezugwu, H. Ye, and G. Fanchini, Nanoscale **7**, 252 (2015).

[81] D. Denkova, N. Verellen, A. V. Silhanek, V. K. Valev, P. Van Dorpe, and V. V. Moshchalkov, ACS Nano **7**, 3168 (2013).

[82] S. Hunsche, M. Koch, I. Brener, and M. . Nuss, Opt. Commun. **150**, 22 (1998).

[83] A. Lahrech, R. Bachelot, P. Gleyzes, and A. C. Boccara, Opt. Lett. **21**, 1315 (1996).

[84] O. Cathabard, R. Teissier, J. Devenson, J. C. Moreno, and A. N. Baranov, Appl. Phys. Lett. **96**, 4 (2010).

[85] C. Walther, M. Fischer, G. Scalari, R. Terazzi, N. Hoyler, and J. Faist, Appl. Phys. Lett. **91**, 2005 (2007).

[86] J. Döring, H.-G. von Ribbeck, M. Fehrenbacher, S. C. Kehr, and L. M. Eng, Appl. Phys. Lett. **105**, 053109 (2014).

[87] T. J. Huffman, D. J. Lahneman, S. L. Wang, T. Slusar, B.-J. Kim, H.-T. Kim, and M. M. Qazilbash, Phys. Rev. B **97**, 085146 (2018).

[88] A. J. Frenzel, A. S. McLeod, D. Z.-R. Wang, Y. Liu, W. Lu, G. Ni, A. W. Tsen, Y. Sun, A. N. Pasupathy, and D. N. Basov, Phys. Rev. B **97**, 035111 (2018).

[89] S. N. Gilbert Corder, X. Chen, S. Zhang, F. Hu, J. Zhang, Y. Luan, J. A. Logan, T. Ciavatti, H. A. Bechtel, M. C. Martin, M. Aronson, H. S. Suzuki, S. Kimura, T. Iizuka, Z. Fei, K. Imura, N. K. Sato, T. H. Tao, and M. Liu, Nat. Commun. **8**, 2262 (2017).

[90] S. N. Gilbert Corder, J. Jiang, X. Chen, S. Kittiwatanakul, I.-C. Tung, Y. Zhu, J. Zhang, H. A. Bechtel, M. C. Martin, G. L. Carr, J. Lu, S. A. Wolf, H. Wen, T. H. Tao, and M. Liu, Phys. Rev. B **96**, 161110 (2017).

[91] M. M. Qazilbash, M. Brehm, G. O. Andreev, A. Frenzel, P.-C. Ho, B.-G. Chae, B.-J. Kim, S. J. Yun, H.-T. Kim, A. V Balatsky, O. G. Shpyrko, M. B. Maple, F. Keilmann, and D. N. Basov, Phys. Rev. B **79**, 075107 (2009).

[92] A. Frenzel, M. M. Qazilbash, M. Brehm, B.-G. Chae, B.-J. Kim, H.-T. Kim, A. V Balatsky, F. Keilmann, and D. N. Basov, Phys. Rev. B **80**, 115115 (2009).

[93] Q. Jia, J. Grenzer, H. He, W. Anwand, Y. Ji, Y. Yuan, K. Huang, T. You, W. Yu, W. Ren, X. Chen, M. Liu, S. Facsko, X. Wang, and X. Ou, Adv. Mater. Interfaces **1701268**, 1701268 (2018).

[94] J. M. Atkin, S. Berweger, A. C. Jones, and M. B. Raschke, Adv. Phys. **61**, 745 (2012).

[95] A. C. Jones, S. Berweger, J. Wei, D. Cobden, and M. B. Raschke, Nano Lett. **10**, 1574 (2010).

[96] M. K. Liu, M. Wagner, E. Abreu, S. Kittiwatanakul, A. McLeod, Z. Fei, M. Goldflam, S. Dai, M. M. Fogler, J. Lu, S. A. Wolf, R. D. Averitt, and D. N. Basov, Phys. Rev. Lett. **111**, 096602 (2013).

[97] A. Charnukha, A. Cvitkovic, T. Prokscha, D. Pröpper, N. Ocelic, A. Suter, Z. Salman, E. Morenzoni, J. Deisenhofer, V. Tsurkan, A. Loidl, B. Keimer, and A. V. Boris, Phys. Rev. Lett. **109**, 017003 (2012).

[98] M. Liu, M. Wagner, J. Zhang, A. McLeod, S. Kittiwatanakul, Z. Fei, E. Abreu, M. Goldflam, A. J. Sternbach, S. Dai, K. G. West, J. Lu, S. A. Wolf, R. D. Averitt, and D. N. Basov, Appl. Phys. Lett. **104**, 1 (2014).

[99] M. Liu, A. J. Sternbach, and D. N. Basov, Reports Prog. Phys. **80**, 014501 (2017).

[100] M. Liu, A. J. Sternbach, M. Wagner, T. V Slusar, T. Kong, S. L. Bud, S. Kittiwatanakul, M. M. Qazilbash, A. Mcleod, Z. Fei, E. Abreu, J. Zhang, M. Goldflam, S. Dai, G. Ni, J. Lu, H. A. Bechtel, M. C. Martin, M. B. Raschke, R. D. Averitt, S. A. Wolf, H. Kim, P. C. Canfield, and D. N. Basov, Phys. Rev. B Condens. Matter Mater. Phys. **91**, 245155 (2015).

[101] X. Lu, O. Khatib, X. Du, J. Duan, W. Wei, X. Liu, H. A. Bechtel, F. D'Apuzzo, M. Yan, A. Buyanin, Q. Fu, J. Chen, M. Salmeron, J. Zeng, M. B. Raschke, P. Jiang, and X. Bao, Adv. Electron. Mater. **4**, 1700377 (2018).

[102] K. S. Kim, D. Trajanoski, K. Ho, L. Gilburd, A. Maiti, L. Van Der Velden, S. De Beer, and G. C. Walker, J. Phys. Chem. Lett. **8**, 2902 (2017).

[103] J. A. Gerber, S. Berweger, B. T. O'Callahan, and M. B. Raschke, Phys. Rev. Lett. **113**, 055502 (2014).

[104] A. Woessner, M. B. Lundeberg, Y. Gao, A. Principi, P. Alonso-González, M. Carrega, K. Watanabe, T. Taniguchi, G. Vignale, M. Polini, J. Hone, R. Hillenbrand, and F. H. L. Koppens, Nat. Mater. **14**, 421 (2015).

[105] Z. Shi, H. A. Bechtel, S. Berweger, Y. Sun, B. Zeng, C. Jin, H. Chang, M. C. Martin, M. B. Raschke, and F. Wang, ACS Photonics **2**, 790 (2015).

[106] X. G. Xu, J. H. Jiang, L. Gilburd, R. G. Rensing, K. S. Burch, C. Zhi, Y. Bando, D. Golberg, and G. C. Walker, ACS Nano **8**, 11305 (2014).

[107] X. G. Xu, A. E. Tanur, and G. C. Walker, J. Phys. Chem. A **117**, 3348 (2013).

[108] F. Hu, Y. Luan, M. E. Scott, J. Yan, D. G. Mandrus, X. Xu, and Z. Fei, Nat. Photonics **11**, 356 (2017).

[109] D. Hu, X. Yang, C. Li, R. Liu, Z. Yao, H. Hu, S. N. G. Corder, J. Chen, Z. Sun, M. Liu, and Q. Dai, Nat. Commun. **8**, (2017).

[110] T. Low, A. Chaves, J. D. Caldwell, A. Kumar, N. X. Fang, P. Avouris, T. F. Heinz, F. Guinea, L. Martin-Moreno, and F. Koppens, Nat. Mater. **16**, 182 (2017).

[111] J.-H. Jiang, X. G. Xu, L. Gilburd, and G. C. Walker, Opt. Express **25**, 25059 (2017).

[112] D. N. Basov, M. M. Fogler, and F. J. Garcia de Abajo, Science (80-.). **354**, aag1992 (2016).

[113] F. J. Alfaro-Mozaz, P. Alonso-González, S. Vélez, I. Dolado, M. Autore, S. Mastel, F. Casanova, L. E. Hueso, P. Li, A. Y. Nikitin, and R. Hillenbrand, Nat. Commun. **8**, 15624 (2017).

[114] P. Li, I. Dolado, F. J. Alfaro-Mozaz, F. Casanova, L. E. Hueso, S. Liu, J. H. Edgar, A. Y. Nikitin, S. Vélez, and R. Hillenbrand, Science (80-.). **359**, 892 (2018).

[115] F. J. Bezares, A. De Sanctis, J. R. M. Saavedra, A. Woessner, P. Alonso-González, I. Amenabar, J. Chen, T. H. Bointon, S. Dai, M. M. Fogler, D. N. Basov, R. Hillenbrand, M. F. Craciun, F. J. García de Abajo, S. Russo, and F. H. L. Koppens, Nano Lett. **17**, 5908 (2017).

[116] Z. Shi, X. Hong, H. A. Bechtel, B. Zeng, M. C. Martin, K. Watanabe, T. Taniguchi, Y.-R. Shen, and F. Wang, Nat. Photonics **9**, 515 (2015).

[117] E. Yoxall, M. Schnell, A. Y. Nikitin, O. Txoperena, A. Woessner, M. B. Lundeberg, F. Casanova, L. E. Hueso, F. H. L. Koppens, and R. Hillenbrand, Nat. Photonics **9**, 674 (2015).

[118] J. Duan, R. Chen, Y. Cheng, T. Yang, F. Zhai, Q. Dai, and J. Chen, Adv. Mater. **1800367**, 1800367 (2018).

[119] A. M. Dubrovkin, B. Qiang, H. N. S. Krishnamoorthy, N. I. Zheludev, and Q. J. Wang, Nat. Commun. **9**, 1762 (2018).

[120] A. Woessner, Y. Gao, I. Torre, M. B. Lundeberg, C. Tan, K. Watanabe, T. Taniguchi, R. Hillenbrand, J. Hone, M. Polini, and F. H. L. Koppens, Nat. Photonics **11**, 421 (2017).

[121] Q. Xu, T. Ma, M. Danesh, B. N. Shivananju, S. Gan, J. Song, C.-W. Qiu, H.-M. Cheng, W. Ren, and Q. Bao, Light Sci. Appl. **6**, e16204 (2016).

[122] Z. Zheng, J. Chen, Y. Wang, X. Wang, X. Chen, P. Liu, J. Xu, W. Xie, H. Chen, S. Deng, and N. Xu, Adv. Mater. **30**, 1705318 (2018).

[123] J. Ehlermann, S. Fohrmann, J. Siebels, and S. Mendach, Phys. Rev. B **91**, 235404 (2015).

[124] B. Y. Jiang, G. X. Ni, C. Pan, Z. Fei, B. Cheng, C. N. Lau, M. Bockrath, D. N. Basov, and M. M. Fogler, Phys. Rev. Lett. **117**, 1 (2016).

[125] Z. Fei, E. G. Iwinski, G. X. Ni, L. M. Zhang, W. Bao, A. S. Rodin, Y. Lee, M. Wagner, M. K. Liu, S. Dai, M. D. Goldflam, M. Thiemens, F. Keilmann, C. N. Lau, A. H. Castro-Neto, M. M. Fogler, and D. N. Basov, Nano Lett. **15**, 4973 (2015).

[126] Z. Fei, A. S. S. Rodin, W. Gannett, S. Dai, W. Regan, M. Wagner, M. K. K. Liu, A. S. S. McLeod, G. Dominguez, M. Thiemens, A. H. H. Castro Neto, F. Keilmann, A. Zettl, R. Hillenbrand, M. M. M. Fogler, and D. N. N. Basov, Nat. Nanotechnol. **8**, 821 (2013).

[127] Z. Fei, M. D. Goldflam, J.-S. Wu, S. Dai, M. Wagner, A. S. McLeod, M. K. Liu, K. W. Post, S. Zhu, G. C. A. M. Janssen, M. M. Fogler, and D. N. Basov, Nano Lett. **15**, 8271 (2015).

[128] S. Dai, Q. Ma, M. K. Liu, T. Andersen, Z. Fei, M. D. Goldflam, M. Wagner, K. Watanabe, T. Taniguchi, M. Thiemens, F. Keilmann, G. C. a. M. Janssen, S.-E. Zhu, P. Jarillo-Herrero, M. M. Fogler, and D. N. Basov, Nat. Nanotechnol. **10**, 682 (2015).

[129] Y. Bao, S. Zu, W. Liu, L. Zhou, X. Zhu, and Z. Fang, Phys. Rev. B **95**, 081406 (2017).

[130] A. García-Etxarri, I. Romero, F. J. García de Abajo, R. Hillenbrand, and J. Aizpurua, Phys. Rev. B **79**, 125439 (2009).

[131] D.-S. Kim and Z. H. Kim, Opt. Express **20**, 8689 (2012).

[132] P. Alonso-González, P. Albella, F. Neubrech, C. Huck, J. Chen, F. Golmar, F. Casanova, L. E. Hueso, A. Pucci, J. Aizpurua, and R. Hillenbrand, Phys. Rev. Lett. **110**, 1 (2013).

[133] J. A. Schuller, E. S. Barnard, W. Cai, Y. C. Jun, J. S. White, and M. L. Brongersma, Nat. Mater. **9**, 193 (2010).

[134] R. Hillenbrand and F. Keilmann, Appl. Phys. B Lasers Opt. **73**, 239 (2001).

[135] P. Alonso-Gonzalez, M. Schnell, P. Sarriugarte, H. Sobhani, C. Wu, N. Arju, A. Khanikaev, F. Golmar, P. Albella, L. Arzubiaga, F. Casanova, L. E. Hueso, P. Nordlander, G. Shvets, and R. Hillenbrand, Nano Lett. **11**, 3922 (2011).

[136] M. Rahmani, E. Yoxall, B. Hopkins, Y. Sonnefraud, Y. Kivshar, M. Hong, C. Phillips, S. A. Maier, and A. E. Miroshnichenko, ACS Nano **7**, 11138 (2013).

[137] W. Chen, A. Kimel, A. Kirilyuk, and T. Rasing, Phys. Status Solidi Basic Res. **247**, 2047 (2010).

[138] Y. Xu, E. Tucker, G. Boreman, M. B. Raschke, and B. A. Lail, ACS Photonics **3**, 881 (2016).

[139] J. Dorfmüller, D. Dregely, M. Esslinger, W. Khunsin, R. Vogelgesang, K. Kern, and

H. Giessen, Nano Lett. **11**, 2819 (2011).

[140] T. G. Habteyes, J. Phys. Chem. C **118**, 9119 (2014).

[141] S. E. Grefe, D. Leiva, S. Mastel, S. D. Dhuey, S. Cabrini, P. J. Schuck, and Y. Abate, Phys. Chem. Chem. Phys. **15**, 18944 (2013).

[142] H. T. Stinson, J. S. Wu, B. Y. Jiang, Z. Fei, a. S. Rodin, B. C. Chapler, a. S. McLeod, A. Castro Neto, Y. S. Lee, M. M. Fogler, and D. N. Basov, Phys. Rev. B **90**, 014502 (2014).

[143] A. Arcangeli, F. Rossella, A. Tomadin, J. Xu, D. Ercolani, L. Sorba, F. Beltram, A. Tredicucci, M. Polini, and S. Roddaro, Nano Lett. **16**, 5688 (2016).

[144] V. Suresh, L. Ding, A. B. Chew, and F. L. Yap, ACS Appl. Nano Mater. **1**, 886 (2018).

[145] E. Ostrovsky, K. Cohen, S. Tsesses, B. Gjonaj, and G. Bartal, Optica **5**, 283 (2018).

[146] Y. Sang, X. Wu, S. S. Raja, C.-Y. Wang, H. Li, Y. Ding, D. Liu, J. Zhou, H. Ahn, S. Gwo, and J. Shi, Adv. Opt. Mater. **1701368**, 1701368 (2018).

[147] M. Schnell, P. Sarriugarte, T. Neuman, A. B. Khanikaev, G. Shvets, J. Aizpurua, and R. Hillenbrand, Nano Lett. **16**, 663 (2016).

[148] B. J. Bohn, M. Schnell, M. A. Kats, F. Aieta, R. Hillenbrand, and F. Capasso, Nano Lett. **15**, 3851 (2015).

[149] R. Hillenbrand and F. Keilmann, Appl. Phys. Lett. **80**, 25 (2002).

[150] J. M. Stiegler, Y. Abate, A. Cvitkovic, Y. E. Romanyuk, A. J. Huber, S. R. Leone, and R. Hillenbrand, ACS Nano **5**, 6494 (2011).

[151] J. Chen, P. Albella, Z. Pirzadeh, P. Alonso-González, F. Huth, S. Bonetti, V. Bonanni, J. Åkerman, J. Nogués, P. Vavassori, A. Dmitriev, J. Aizpurua, and R. Hillenbrand, Small **7**, 2341 (2011).

[152] Z. Nuño, B. Hessler, B. Heiberg, R. Damato, T. Dunlap, Y.-S. Shon, and Y. Abate, J. Nanoparticle Res. **14**, 776 (2012).

[153] N. F. Mott, Rev. Mod. Phys. **40**, 677 (1968).

[154] E. Dagotto, Science (80-.). **309**, 257 (2005).

[155] B. T. O'Callahan and M. B. Raschke, APL Photonics **2**, 021301 (2017).

[156] A. A. Govyadinov, S. Mastel, F. Golmar, A. Chuvilin, P. S. Carney, and R. Hillenbrand, ACS Nano **8**, 6911 (2014).

[157] A. a. Govyadinov, I. Amenabar, F. Huth, P. S. Carney, and R. Hillenbrand, J. Phys. Chem. Lett. **4**, 1526 (2013).

[158] D. E. Tranca, S. G. Stanciu, R. Hristu, C. Stoichita, S. a M. Tofail, and G. a Stanciu,

Sci. Rep. **5**, 11876 (2015).

[159] C. Liao and Y. Lo, J. Opt. Soc. Am. B **30**, 2819 (2013).

[160] D. E. Tranca, S. G. Stanciu, R. Hristu, B. M. Witgen, and G. A. Stanciu, Nanomedicine Nanotechnology, Biol. Med. **14**, 47 (2018).

[161] J. Aizpurua, T. Taubner, F. J. García de Abajo, M. Brehm, and R. Hillenbrand, Opt. Express **16**, 1529 (2008).

[162] P. Li, T. Wang, H. Böckmann, and T. Taubner, Nano Lett. **14**, 4400 (2014).

[163] L. Wang and X. G. Xu, Nat. Commun. **6**, 8973 (2015).

[164] H. Wang, L. Wang, D. S. Jakob, and X. G. Xu, AIP Adv. **7**, 055118 (2017).

[165] J. Orenstein, Phys. Today **65**, 44 (2012).

[166] R. Ulbricht, E. Hendry, J. Shan, T. F. Heinz, and M. Bonn, Rev. Mod. Phys. **83**, 543 (2011).

[167] A. J. Sternbach, J. Hinton, T. Slusar, A. S. McLeod, M. K. Liu, A. Frenzel, M. Wagner, R. Iraheta, F. Keilmann, A. Leitenstorfer, M. Fogler, H.-T. Kim, R. D. Averitt, and D. N. Basov, Opt. Express **25**, 28589 (2017).

[168] M. Wagner, Z. Fei, A. S. McLeod, A. S. Rodin, W. Bao, E. G. Iwinski, Z. Zhao, M. Goldflam, M. Liu, G. Dominguez, M. Thiemens, M. M. Fogler, A. H. Castro Neto, C. N. Lau, S. Amarie, F. Keilmann, and D. N. Basov, Nano Lett. **14**, 894 (2014).

[169] M. Wagner, A. S. McLeod, S. J. Maddox, Z. Fei, M. Liu, R. D. Averitt, M. M. Fogler, S. R. Bank, F. Keilmann, and D. N. Basov, Nano Lett. **14**, 4529 (2014).

[170] B. T. O'Callahan, A. C. Jones, J. Hyung Park, D. H. Cobden, J. M. Atkin, and M. B. Raschke, Nat. Commun. **6**, 6849 (2015).

[171] S. A. Dönges, O. Khatib, B. T. O'Callahan, J. M. Atkin, J. H. Park, D. Cobden, and M. B. Raschke, Nano Lett. **16**, 3029 (2016).

[172] H. Wang, L. Wang, and X. G. Xu, Nat. Commun. **7**, 13212 (2016).

[173] R. Jacob, S. Winnerl, H. Schneider, M. Helm, M. T. Wenzel, H.-G. von Ribbeck, L. M. Eng, and S. C. Kehr, Opt. Express **18**, 26206 (2010).

[174] Z. Fei, G. O. Andreev, W. Bao, L. M. Zhang, A. S. McLeod, C. Wang, M. K. Stewart, Z. Zhao, G. Dominguez, M. Thiemens, M. M. Fogler, M. J. Tauber, A. H. Castro-Neto, C. N. Lau, F. Keilmann, and D. N. Basov, Nano Lett. **11**, 4701 (2011).

[175] J. Mattis Hoffmann, B. Hauer, and T. Taubner, Appl. Phys. Lett. **101**, (2012).

[176] P. Hermann, A. Hoehl, P. Patoka, F. Huth, E. Rühl, G. Ulm, P. Hermanna, P. Patoka, F. Huthe, E. Rtihl, G. Virna, and F. Vniversitat, Opt. Express **21**, 2913 (2013).

[177] C. M. Johnson and M. Böhmler, Corros. Sci. **108**, 60 (2016).

[178] P. Hermann, B. Kästner, A. Hoehl, V. Kashcheyevs, P. Patoka, G. Ulrich, J. Feikes, M. Ries, T. Tydecks, B. Beckhoff, E. Rühl, and G. Ulm, Opt. Express **25**, 16574 (2017).

[179] B. Pollard, F. C. B. Maia, M. B. Raschke, and R. O. Freitas, Nano Lett. **16**, 55 (2016).

[180] I. Amenabar, S. Poly, M. Goikoetxea, W. Nuansing, P. Lasch, and R. Hillenbrand, Nat. Commun. **8**, 14402 (2017).

[181] P. Patoka, G. Ulrich, A. E. Nguyen, L. Bartels, P. A. Dowben, V. Turkowski, T. S. Rahman, P. Hermann, B. Kästner, A. Hoehl, G. Ulm, and E. Rühl, Opt. Express **24**, 1154 (2016).

[182] L. M. Zhang, G. O. Andreev, Z. Fei, A. S. McLeod, G. Dominguez, M. Thiemens, A. H. Castro-Neto, D. N. Basov, and M. M. Fogler, Phys. Rev. B **85**, 075419 (2012).

[183] P. Hermann, A. Hoehl, G. Ulrich, C. Fleischmann, A. Hermelink, B. Kästner, P. Patoka, A. Hornemann, B. Beckhoff, E. Rühl, and G. Ulm, Opt. Express **22**, 17948 (2014).

[184] S. Kimura and H. Okamura, J. Phys. Soc. Japan **82**, 1 (2012).

[185] J. Feikes, M. Von Hartrott, M. Ries, P. Schmid, G. Wüstefeld, A. Hoehl, R. Klein, R. Müller, and G. Ulm, Phys. Rev. Spec. Top. - Accel. Beams **14**, 1 (2011).

[186] R. O. Freitas, F. C. B. Maia, C. Deneke, T. Moreno, P. Dumas, H. Westfahl, and Y. Petroff, Synchrotron Radiat. News **30**, 24 (2017).

[187] G. Kamel, S. Lefrançois, M. Al-Najdawi, T. Abu-Hanieh, I. Saleh, Y. Momani, and P. Dumas, Synchrotron Radiat. News **30**, 8 (2017).

[188] R. O. Freitas, C. Deneke, F. C. B. Maia, H. G. Medeiros, T. Moreno, P. Dumas, Y. Petroff, and H. Westfahl, Opt. Express **26**, 11238 (2018).

[189] O. Khatib, H. A. Bechtel, M. C. Martin, M. B. Raschke, and G. L. Carr, ACS Photonics acsphotonics.8b00565 (2018).

[190] D. J. Lahneman, T. J. Huffman, P. Xu, S. L. Wang, T. Grogan, and M. M. Qazilbash, Opt. Express **25**, 20421 (2017).

[191] M. Wagner, D. S. Jakob, S. Horne, H. Mittel, S. Osechinskiy, C. Phillips, G. C. Walker, C. Su, and X. G. Xu, ACS Photonics acsphotonics.7b01484 (2018).

[192] P. H. Siegel, IEEE Trans. Microw. Theory Tech. **52**, 2438 (2004).

[193] A. J. Fitzgerald, V. P. Wallace, M. Jimenez-Linan, L. Bobrow, R. J. Pye, A. D. Purushotham, and D. D. Arnone, Radiology **239**, 533 (2006).

[194] C. Jansen, S. Wietzke, O. Peters, M. Scheller, N. Vieweg, M. Salhi, N. Krumbholz, C.

Jördens, T. Hochrein, and M. Koch, Appl. Opt. **49**, E48 (2010).

[195] Z. Zhou, T. Zhou, S. Zhang, Z. Shi, Y. Chen, W. Wan, X. Li, X. Chen, S. N. Gilbert Corder, Z. Fu, L. Chen, Y. Mao, J. Cao, F. G. Omenetto, M. Liu, H. Li, and T. H. Tao, Adv. Sci. **1700982**, 1700982 (2018).

[196] R. A. Lewis, Proc. IEEE **95**, 1641 (2007).

[197] D. W. Faries, P. L. Richards, Y. R. Shen, and K. H. Yang, Phys. Rev. A **3**, 2148 (1971).

[198] Q. Y. Lu, N. Bandyopadhyay, S. Slivken, Y. Bai, and M. Razeghi, Appl. Phys. Lett. **103**, (2013).

[199] B. S. Williams, S. Kumar, H. Callebaut, and J. L. Reno, 16th Annu. Meet. IEEE Lasers Electro-Optics Soc. 2003. LEOS 2003. **1**, 342 (2003).

[200] S. Kumar, B. S. Williams, S. Kohen, Q. Hu, and J. L. Reno, Appl. Phys. Lett. **84**, 2494 (2004).

[201] K. Wang, D. M. Mittleman, N. C. J. Van Der Valk, and P. C. M. Planken, Appl. Phys. Lett. **85**, 2715 (2004).

[202] H. Zhan, V. Astley, M. Hvasta, J. A. Deibel, D. M. Mittleman, and Y. S. Lim, Appl. Phys. Lett. **91**, 2 (2007).

[203] K. Wang, A. Barkan, and D. M. Mittleman, Appl. Phys. Lett. **84**, 305 (2004).

[204] V. Astley, H. Zhan, R. Mendis, and D. M. Mittleman, J. Appl. Phys. **105**, 24 (2009).

[205] H. Zhan, R. Mendis, and D. M. Mittleman, J. Opt. Soc. Am. B **28**, 558 (2011).

[206] J. Liu, R. Mendis, D. M. Mittleman, and N. Sakoda, Appl. Phys. Lett. **100**, 031101 (2012).

[207] H.-G. von Ribbeck, M. Brehm, D. W. van der Weide, S. Winnerl, O. Drachenko, M. Helm, and F. Keilmann, Opt. Express **16**, 3430 (2008).

[208] R. Jacob, S. Winnerl, M. Fehrenbacher, J. Bhattacharyya, H. Schneider, M. T. Wenzel, H.-G. von Ribbeck, L. M. Eng, P. Atkinson, O. G. Schmidt, and M. Helm, Nano Lett. **12**, 4336 (2012).

[209] Q. Chen, Z. Jiang, G. X. Xu, and X. C. Zhang, Opt. Lett. **25**, 1122 (2000).

[210] H.-T. Chen, R. Kersting, and G. C. Cho, Appl. Phys. Lett. **83**, 3009 (2003).

[211] P. R. Smith, D. H. Auston, and M. C. Nuss, IEEE J. Quantum Electron. **24**, 255 (1988).

[212] N. Katzenellenbogen and D. Grischkowsky, Appl. Phys. Lett. **58**, 222 (1991).

[213] Y. C. Shen, P. C. Upadhya, H. E. Beere, E. H. Linfield, A. G. Davies, I. S. Gregory, C. Baker, W. R. Tribe, and M. J. Evans, Appl. Phys. Lett. **85**, 164 (2004).

[214] T. Kurihara, K. Yamaguchi, H. Watanabe, M. Nakajima, and T. Suemoto, Appl. Phys. Lett. **103**, 151105 (2013).

[215] K. Moon, H. Park, J. Kim, Y. Do, S. Lee, G. Lee, H. Kang, and H. Han, Nano Lett. **15**, 549 (2015).

[216] C. Liewald, S. Mastel, J. Hesler, A. J. Huber, R. Hillenbrand, and F. Keilmann, Optica **5**, 159 (2018).

[217] P. Alonso-González, A. Y. Nikitin, Y. Gao, A. Woessner, M. B. Lundeberg, A. Principi, N. Forcellini, W. Yan, S. Vélez, A. J. Huber, K. Watanabe, T. Taniguchi, F. Casanova, L. E. Hueso, M. Polini, J. Hone, F. H. L. Koppens, and R. Hillenbrand, Nat. Nanotechnol. **12**, 31 (2016).

[218] M. B. Lundeberg, Y. Gao, R. Asgari, C. Tan, B. Van Duppen, M. Autore, P. Alonso-González, A. Woessner, K. Watanabe, T. Taniguchi, R. Hillenbrand, J. Hone, M. Polini, and F. H. L. Koppens, Science (80-.). **357**, 187 (2017).

[219] P. Klarskov, H. Kim, V. L. Colvin, and D. M. Mittleman, ACS Photonics **4**, 2676 (2017).

[220] H. U. Yang, E. Hebestreit, E. E. Josberger, and M. B. Raschke, Rev. Sci. Instrum. **84**, 023701 (2013).

[221] G. X. Ni, A. S. McLeod, Z. Sun, L. Wang, L. Xiong, K. W. Post, S. S. Sunku, B.-Y. Jiang, J. Hone, C. R. Dean, M. M. Fogler, and D. N. Basov, Nature **557**, 530 (2018).

[222] K. Lai, M. Nakamura, W. Kundhikanjana, M. Kawasaki, Y. Tokura, M. A. Kelly, and Z.-X. Shen, Science (80-.). **329**, 190 (2010).

[223] K. Lai, W. Kundhikanjana, M. Kelly, and Z. X. Shen, Rev. Sci. Instrum. **79**, 063703 (2008).

[224] G. Gramse, M. Kasper, L. Fumagalli, G. Gomila, P. Hinterdorfer, and F. Kienberger, Nanotechnology **25**, 145703 (2014).

[225] K. Lai, W. Kundhikanjana, H. Peng, Y. Cui, M. A. Kelly, and Z. X. Shen, Rev. Sci. Instrum. **80**, 043707 (2009).

[226] W. Dickson, S. Takahashi, R. Pollard, R. Atkinson, and a V Zayats, J. Microsc. **209**, 194 (2003).

[227] J. N. Walford, J.-A. Porto, R. Carminati, and J.-J. Greffet, J. Opt. Soc. Am. A **19**, 572 (2002).

[228] W. Dickson, A. Stashkevitch, J. Ben Youssef, S. Takahashi, and A. V. Zayats, Opt. Commun. **250**, 126 (2005).

[229] P. L. Stiles, J. A. Dieringer, N. C. Shah, and R. P. Van Duyne, Annu. Rev. Anal. Chem. **1**, 601 (2008).

[230] X. Shi, N. Coca-López, J. Janik, and A. Hartschuh, Chem. Rev. **117**, 4945 (2017).

[231] W. Zhang, Z. Fang, and X. Zhu, Chem. Rev. **117**, 5095 (2017).

[232] P. Kusch, S. Mastel, N. S. Mueller, N. Morquillas Azpiazu, S. Heeg, R. Gorbachev, F. Schedin, U. Hübner, J. I. Pascual, S. Reich, and R. Hillenbrand, Nano Lett. **17**, 2667 (2017).

[233] F. Pfeiffer, C. David, J. F. van der Veen, and C. Bergemann, Phys. Rev. B **73**, 245331 (2006).

[234] J. Park, Q. Zhang, P. Chen, M. P. Cosgriff, J. A. Tilka, C. Adamo, D. G. Schlom, H. Wen, Y. Zhu, and P. G. Evans, Rev. Sci. Instrum. **86**, 0 (2015).

[235] G. Dai, Z. Yang, G. Geng, M. Li, T. Chang, D. Wei, C. Du, H.-L. Cui, and H. Wang, Appl. Spectrosc. Rev. **4928**, 1 (2018).

[236] B. Deutsch, R. Hillenbrand, and L. Novotny, Opt. Express **16**, 494 (2008).

[237] M. Schnell, P. S. Carney, and R. Hillenbrand, Nat. Commun. **5**, 1 (2014).

[238] B. Deutsch, M. Schnell, R. Hillenbrand, and P. S. Carney, Opt. Express **22**, 26621 (2014).

[239] X. G. Xu, L. Gilburd, and G. C. Walker, Appl. Phys. Lett. **105**, 263104 (2014).

[240] I. Stefanon, S. Blaize, A. Bruyant, S. Aubert, G. Lerondel, R. Bachelot, and P. Royer, Opt. Expr. **13**, 5553 (2005).

[241] L. Gomez, R. Bachelot, A. Bouhelier, G. P. Wiederrecht, S. Chang, S. K. Gray, F. Hua, S. Jeon, J. a. Rogers, M. E. Castro, S. Blaize, I. Stefanon, G. Lerondel, and P. Royer, J. Opt. Soc. Am. B **23**, 823 (2006).

[242] J. E. Hall, G. P. Wiederrecht, S. K. Gray, S.-H. Chang, S. Jeon, J. a Rogers, R. Bachelot, and P. Royer, Opt. Express **15**, 4098 (2007).

[243] N. Ocelic, A. Huber, and R. Hillenbrand, Appl. Phys. Lett. **89**, 101124 (2006).

[244] D. E. Tranca, C. Stoichita, R. Hristu, S. G. Stanciu, and G. A. Stanciu, Opt. Express **22**, 1687 (2014).

[245] C. Moreno, J. Alda, E. Kinzel, and G. Boreman, Appl. Opt. **56**, 1037 (2017).

[246] E. Wolf and M. Nieto-Vesperinas, J. Opt. Soc. Am. A **2**, 886 (1985).

[247] G. W. Ford and W. H. Weber, Phys. Rep. **113**, 195 (1984).

[248] Z. Fei, (2014).

[249] A. S. McLeod, P. Kelly, M. D. Goldflam, Z. Gainsforth, A. J. Westphal, G. Dominguez, M. H. Thiemens, M. M. Fogler, and D. N. Basov, Phys. Rev. B **90**, 085136 (2014).

[250] R. K. Moore and W. E. Blair, J. Res. Natl. Bur. Stand. Sect. D Radio Propag. **65D**, 547 (1961).

[251] P. R. Antoniewicz, J. Chem. Phys. **56**, 1711 (1972).

[252] P. A. Bobbert and J. Vlieger, Phys. A Stat. Mech. Its Appl. **137**, 209 (1986).

[253] B. R. Johnson, J. Opt. Soc. Am. A **9**, 1341 (1992).

[254] R. Schmehl, Arizona State Univ. Dept. Mech. … 1 (1994).

[255] P. C. Chaumet and M. Nieto-Vesperinas, Phys. Rev. B **61**, 14119 (2000).

[256] F. Zenhausern, Y. Martin, and H. K. Wickramasinghe, Science (80-.). **269**, 1083 (1995).

[257] R. Hillenbrand and F. Keilmann, Phys. Rev. Lett. **85**, 3029 (2000).

[258] R. Hillenbrand, B. Knoll, and F. Keilmann, J. Microsc. **202**, 77 (2001).

[259] J. Renger, S. Grafström, L. M. Eng, and R. Hillenbrand, Phys. Rev. B **71**, 075410 (2005).

[260] K. Moon, E. Jung, M. Lim, Y. Do, and H. Han, Opt. Express **19**, 11539 (2011).

[261] E. Yoxall, M. Navarro-Cía, M. Rahmani, S. A. Maier, and C. C. Phillips, Appl. Phys. Lett. **103**, 213110 (2013).

[262] C. Bohren and D. Huffman, *Absorption and Scattering of Light by Small Particles* (John Wiley & Sons, 2008).

[263] I. S. Averbukh, B. M. Chernobrod, O. A. Sedletsky, and Y. Prior, Opt. Commun. **174**, 33 (2000).

[264] S. C. Schneider, S. Grafström, and L. M. Eng, Phys. Rev. B **71**, 115418 (2005).

[265] J. A. Porto, P. Johansson, S. P. Apell, and T. López-Ríos, Phys. Rev. B **67**, 085409 (2003).

[266] S. V. Sukhov, Ultramicroscopy **101**, 111 (2004).

[267] A. Cvitkovic, N. Ocelic, and R. Hillenbrand, Opt. Express **15**, 8550 (2007).

[268] I. V. Lindell and K. I. Nikoskinen, J. Electromagn. Waves Appl. **15**, 1075 (2001).

[269] S. Amarie and F. Keilmann, Phys. Rev. B **83**, 045404 (2011).

[270] B.-Y. Jiang, L. M. Zhang, A. H. Castro Neto, D. N. Basov, and M. M. Fogler, J. Appl. Phys. **119**, 054305 (2016).

[271] S. T. Chui, X. Chen, M. Liu, Z. Lin, and J. Zi, Phys. Rev. B **97**, 081406 (2018).

[272] X. Chen, C. F. B. Lo, W. Zheng, H. Hu, Q. Dai, and M. Liu, Appl. Phys. Lett. **111**, 223110 (2017).

[273] V. E. Babicheva, G. S, S. M.I, and Y. Abate, **25**, 23935 (2017).

[274] R. Esteban, R. Vogelgesang, and K. Kern, Opt. Express **17**, 2518 (2009).

[275] J. Robertson, Eur. Phys. J. Appl. Phys. **28**, 265 (2004).

[276] M. Skacel, F. Pagliano, T. Hoang, L. Midolo, S. Fattahpoor, L. Li, E. H. Linfield, and A. Fiore, Phys. Rev. B **88**, 035416 (2013).

[277] A. J. Huber, N. Ocelic, and R. Hillenbrand, J. Microsc. **229**, 389 (2008).

[278] A. Dazzi and C. B. Prater, Chem. Rev. **117**, 5146 (2017).

[279] M. Pilling and P. Gardner, Chem. Soc. Rev. **45**, 1935 (2016).

[280] S. Morsch, P. D. Bastidas, and S. M. Rowland, J. Mater. Chem. A **5**, 24508 (2017).

[281] Z. Liu, K. Nørgaard, M. H. Overgaard, M. Ceccato, D. M. A. Mackenzie, N. Stenger, S. L. S. Stipp, and T. Hassenkam, Carbon N. Y. **127**, 141 (2018).

[282] A. L. Bondy, R. M. Kirpes, R. L. Merzel, K. A. Pratt, M. M. Banaszak Holl, and A. P. Ault, Anal. Chem. **89**, 8594 (2017).

[283] L. V. Brown, M. Davanco, Z. Sun, A. Kretinin, Y. Chen, J. R. Matson, I. Vurgaftman, N. Sharac, A. J. Giles, M. M. Fogler, T. Taniguchi, K. Watanabe, K. S. Novoselov, S. A. Maier, A. Centrone, and J. D. Caldwell, Nano Lett. **18**, 1628 (2018).

[284] F. S. Ruggeri, G. Longo, S. Faggiano, E. Lipiec, A. Pastore, and G. Dietler, Nat. Commun. **6**, 1 (2015).

[285] J. Chae, Q. Dong, J. Huang, and A. Centrone, Nano Lett. **15**, 8114 (2015).

[286] F. Lu, M. Jin, and M. A. Belkin, Nat. Photonics **8**, 307 (2014).

[287] S. Ghosh, N. A. Kouamé, L. Ramos, S. Remita, A. Dazzi, A. Deniset-Besseau, P. Beaunier, F. Goubard, P. H. Aubert, and H. Remita, Nat. Mater. **14**, 505 (2015).

[288] A. B. Khanikaev, N. Arju, Z. Fan, D. Purtseladze, F. Lu, J. Lee, P. Sarriugarte, M. Schnell, R. Hillenbrand, M. A. Belkin, and G. Shvets, Nat. Commun. **7**, 1 (2016).

[289] R. Dong, Y. Fang, J. Chae, J. Dai, Z. Xiao, Q. Dong, Y. Yuan, A. Centrone, X. C. Zeng, and J. Huang, Adv. Mater. **27**, 1912 (2015).

[290] B. Lahiri, G. Holland, V. Aksyuk, and A. Centrone, Nano Lett. **13**, 3218 (2013).

[291] J. Yang, J. Hatcherian, P. C. Hackley, and A. E. Pomerantz, Nat. Commun. **8**, 2179 (2017).

[292] S. Komiyama, Y. Kajihara, K. Kosaka, T. Ueda, and Z. An, (2016).

[293] L. Wang, H. Wang, M. Wagner, Y. Yan, D. S. Jakob, and X. G. Xu, Sci. Adv. **3**, e1700255 (2017).

[294] L. Wang, D. Huang, C. K. Chan, Y. J. Li, and X. G. Xu, Chem. Commun. **53**, 7397 (2017).

[295] H. Wang, L. Wang, D. S. Jakob, and X. G. Xu, Nat. Commun. **9**, 2005 (2018).

[296] H. Greener, M. Mrejen, U. Arieli, and H. Suchowski, Opt. Lett. **42**, 3157 (2017).

[297] F. Bilotti, S. Tricarico, F. Pierini, and L. Vegni, Opt. Lett. **36**, 211 (2011).

[298] S. Mastel, M. B. Lundeberg, P. Alonso-González, Y. Gao, K. Watanabe, T. Taniguchi, J. Hone, F. H. L. Koppens, A. Y. Nikitin, and R. Hillenbrand, Nano Lett. **17**, 6526 (2017).

[299] C. C. Neacsu, S. Berweger, R. L. Olmon, L. V. Saraf, C. Ropers, and M. B. Raschke, Nano Lett. **10**, 592 (2010).

[300] T. Umakoshi, Y. Saito, and P. Verma, Nanoscale **8**, 5634 (2016).

[301] H. T. Chorsi and J. X. J. Zhang, IEEE Photonics J. **9**, 1 (2017).

[302] T. Tachizaki, T. Nakata, K. Zhang, I. Yamakawa, and S. Taniguchi, Ultramicroscopy **186**, 18 (2018).

[303] E. A. Power and T. Thirunamachandran, Phys. Rev. A **56**, 3395 (1997).

[304] L. Novotny and B. Hecht, *Principles of Nano-Optics* (Cambridge University Press, Cambridge, 2006).

[305] O. Keller, *Quantum Theory of Near-Field Electrodynamics* (Springer Berlin Heidelberg, Berlin, Heidelberg, 2011).